Crestal graben fluid evolution during growth of the Puig-reig anticline (South Pyrenean fold and thrust belt)

David Cruset [a, b] *, Irene Cantarero [b], Anna Travé [b], Jaume Vergés [a], Cedric M. John [c]

[a] *Group of Dynamics of the Lithosphere, Institute of Earth Sciences Jaume Almera, ICTJA-CSIC, Lluís Solé i Sabaris s/n, 08028 Barcelona, Spain.*
dcruset@ictja.csic.es, jverges@ictja.csic.es

[b] *Departament de Mineralogia, Petrologia i Geologia Aplicada, Universitat de Barcelona, (UB), Martí i Franquès s/n, 08028 Barcelona, Spain.*
i_cantarero@ub.edu, atrave@ub.edu

[c] *Qatar Carbonate and Carbon Storage Research Center and Department of Earth Science and Engineering, Imperial College London, SW7 2BP, UK.*
cedric.john@imperial.ac.uk

* Corresponding author

Abstract

The Puig-reig anticline, located in the South Pyrenean fold and thrust belt, developed during the Alpine compression, which affected the upper Eocene-lower Oligocene sediments of the Solsona and Berga Formations. In this study, we highlight the controls on formation of joints and reverse, strike-slip and normal faults developed in the crest domain of the Puig-reig anticline as well as the relationships between fluids and these fractures. We integrated structural, petrographic and geochemical studies, using for the first time in SE Pyrenees the clumped isotopes thermometry to obtain reliable temperatures of calcite precipitation.

Structural and microstructural analysis demonstrate that at outcrop scale fracturing was controlled by rigidity contrasts between layers, diagenesis and structural position within the anticline, whereas grain size, cementation and porosity controlled deformation at microscopic scale. Petrographic and geochemical studies of calcite precipitated in host rock porosity and fault planes reveal the presence of two migrating fluids, which represents two different stages of evolution of the Puig-reig anticline. During the layer-parallel shortening, hydrothermal fluids with temperatures between 92 and 130^{o}C circulated through the main thrusts to the permeable host rocks, reverse and most of strike-slip faults precipitating as cement Cc1. During the fold growth, meteoric waters circulated downwards through normal and some strike-slip faults and mixed at depth with the previous hydrothermal fluid, precipitating as cement Cc2 at temperatures between 77 and 93ºC.

Integration of the results from the Puig-reig anticline in this work and the El Guix anticline indicates that hydrothermal fluids did not reach the El Guix anticline, in which only meteoric and evolved meteoric waters circulated along the fold.

Keywords: fluids; faults; palaeohydrology; growth anticline; South Pyrenean fold and thrust belt

1. Introduction

A great variety of tectonic, sedimentary and fluid flow interactions take place during deformation of foreland basins at different scales and depths. Thus, fluid-rock interactions during deformation play a significant role during diagenesis, hydrocarbon migration and precipitation of ore deposits as it has been widely recognized (Oliver, 1986; Qing and Mountjoy, 1992; Machel and Cavell, 1999; Dewaele et al., 2004; Roure et al., 2005; Evans and Fischer, 2012; Vandeginste et al., 2012; Beaudoin et al., 2011, 2013, 2014; Lacombe et al., 2014). In addition, diagenetic processes related to fluid flow can control the fracture patterns of rocks (Shackleton et al., 2005; Laubach et al., 2009).

Fluids are expelled into foreland basins by tectonically-induced squeegee fluid flow, using major thrust faults and permeable rocks as paths (Oliver, 1986; Machel and Cavell, 1999; Sibson, 2005). Moreover, other driving forces such as topography and thermal gradients and changes in tectonic stresses and fluid pressures can control fluid flow at basin scale (Oliver, 1986; Heydari, 1997; Bitzer et al., 2001; Lyubetskaya and Ague, 2009). The palaeohydrological history of these fluids (e.g., fluid composition, pressure, temperature and burial) in deformed fold and thrust belts and foreland basins is recorded in the composition of the cements precipitated in rock porosity and fractures (Grant et al., 1990; Banks et al., 1991; McCaig et al., 2000a; Bitzer et al., 2001; Roure et al., 2005). Thus, the study of cements sheds light on the diagenetic and geodynamic evolution of fold and thrust belts.

Joints and faults related to folding in gently deformed foreland basins allow lateral and vertical migration of fluids across different hydrostratigraphic units (Travé et al., 2000; Lefticariu et al., 2005; Fischer et al., 2009; Beaudoin et al., 2011; Barbier et al., 2012; Evans et al., 2012; Evans and Fischer, 2012; Ogata et al., 2014). Previous work on the interactions between folding and fluid flow in fold and thrust belts worldwide have been conducted in many examples such as the Albanian fold and thrust belt (Vilasi et al., 2009), Northern Apennines (Conti et al., 2010), Sicilian fold and thrust belt (Dewever et al., 2013), Appalachians (Srivastava and Engelder, 1990; Evans et al., 2012; Chandonais and Onasch, 2014), Bighorn Basin (Beaudoin et al., 2011, 2013, 2014), Sevier thrust belt (Ogata et al., 2014), Nuncios Fold Complex (Lefticariu et al., 2005; Fischer et al., 2009) and the Zagros fold and thrust belt (Stephenson et al., 2007; Morley et al., 2014).

The South Pyrenean fold and thrust belt and its foreland Ebro basin constitute a well-known and well-preserved case study for tectonic and sedimentary interactions (Vergés et al., 2002a for a review). In this scenario, the study between fluid flow and deformation encompassing a pile of thrust sheets with different ages of emplacement (Vergés et al., 2002b), may contribute to better constrain the large-scale evolution of this fold and thrust belt as well as of its associated foreland basin (e.g., Van Geet et al., 2002; Travé et al., 2004; Ferket et al., 2006; Travé et al., 2007; Dewever et al., 2013; Beaudoin et al., 2014).

A first group of studies regarding the fluid evolution of the south Pyrenees mainly analysed the inner part of the thrust belt in the basement of the Axial Zone (McCaig, 1988; Grant et al., 1990; Banks et al., 1991; Knipe and McCaig, 1994; McCaig et al., 1995; Henderson and McCaig, 1996; McCaig et al., 2000a, b). Furthermore, fluid-rock interactions were analyzed in the cover thrust-sheets along the western side of the Central Pyrenees (Travé et al., 1997, 1998a, 2007; Lacroix et al., 2011; Beaudoin et al., 2015). A few more works report the fluid evolution of the southeastern Pyrenees thrusts sheets and foreland basin further east (Travé et al., 2000) as well as the relationships between fluid flow and hydrocarbon migration during the Eocene (Caja et al., 2006).

The Puig-reig anticline is located along the footwall of the SE Pyrenean outcropping basal thrust (the Vallfogona thrust). This anticline evolved during the late stages of deformation and thus, it was affected by the youngest generations of fluids within the fold and thrust belt system. This fact will permit further comparison with more complex fluid flow scenarios when studying older and piled thrust sheets (Cadí, Lower Pedraforca and Upper Pedraforca thrust sheets).

In this work, we report the fluid flow system evolution during the development of the Puig-reig anticline, located in the eastern sector and frontal most part of the South Pyrenean fold and thrust belt. We integrate structural, petrographic and geochemical data with the aim of determining the origin of the fluids from which cements precipitated in fractures and host rock porosity, and their relationships with deformation. We use for the first time in the southern Pyrenees the clumped isotopes thermometry (Ghosh et al., 2006; Eiler, 2007), which has been recently applied to other fault zones (Swanson et al., 2012; Bergman et al., 2013) allowing to obtain reliable precipitation temperatures when fluid inclusions in calcite does not allow to determine them. Finally, the results from the Puig-reig anticline are compared with the El Guix anticline along the tip-line of the Pyrenean front (Travé et al., 2000, 2007) in order to perform a fluid flow model for the frontal most part of the South Pyrenean fold and thrust belt.

2. Geological setting

The Pyrenees formed by the continental collision between Iberia and Eurasia plates and consist of a doubly verging orogenic belt generated from Late Cretaceous to Oligocene (Muñoz, 2002; Vergés et al., 2002a) (Fig. 1). This collision produced the underthrusting of the Iberian plate below the Eurasian plate as recognised in deep seismic profiles across the orogen (Choukroune et al., 1989; Roure et al., 1989). As a result, the previous Mesozoic extensional basins were inverted and an antiformal stack constituted of basement-involved thrust sheets in the central part of the chain (Axial zone) developed (Muñoz, 1992). To the north of the Axial zone, the thick-skinned North Pyrenean fold and thrust belt was developed whereas to the south, the prevailing structural style was thin-skinned, resulting in the development of the South Pyrenean fold and thrust belt (Fig. 1), detached predominantly above Triassic evaporites (Séguret, 1972) and the Eocene evaporites deposited in the foreland basin (Vergés et al., 1992). During the emplacement of the successive thrust sheets, two foreland basins were formed: the Aquitaine Basin, related to the development of the North Pyrenean fold and thrust belt and the Ebro Basin, related to the emplacement of the South Pyrenean fold and thrust belt (Fig. 1). The Ebro Basin represents the non-marine stage of the South Pyrenean foreland basin (Vergés, 1993) developed from middle Priabonian time (Costa et al., 2010). The fold system deforming the eastern region of the Ebro Basin was detached above the Cardona evaporites (Sans et al., 1996; Sans, 2003). The Puig-reig anticline developed at the northern edge of the Cardona evaporitic basin, with an oblique trend to the Pyrenean direction, and represents a complex ramp anticline between the Beuda and the Cardona thrust flats (Figs. 1 and 2a) (Vergés, 1993).

The Puig-reig anticline is located along the footwall of the SE Pyrenean basal thrust (the Vallfogona thrust) (Figs. 1b and 2). It is a long-wavelength, south-verging and ESE/WNW trending anticline, slightly oblique to the main Pyrenean structures. The anticline is formed above a thrust ramp duplicating middle and upper Eocene marls (Banyoles and Igualada Formations) between the Beuda and the Cardona evaporitic detachment levels (Fig. 2a) (Vergés et al., 1992). The backlimb dips between 5 and 17 degrees towards the north, whereas the forelimb dips up to 40 degrees to the south, being subhorizontal in its frontal part (Fig. 2b). The Oliana anticline is the continuation of the Puig-reig anticline towards the west (Fig. 1), showing a much deeper erosion level, reaching the Igualada marls that are not exposed in the study area.

The stratigraphy of the Puig-reig anticline is composed of Lutetian and Bartonian marine marls (Banyoles and Igualada Formations; Serra-Kiel et al., 2003a, b) followed by non-marine lower-middle Priabonian Berga and Solsona Formations (Riba, 1973; Puigdefàbregas et al., 1986, 1992; Valero et al., 2014). These units represent the endorheic infill of the Ebro basin (García-Castellanos et al., 2003; Sáez et al., 2007; Costa et al., 2010; Fig. 3). The Berga Formation consists of up to 2500 m thick alluvial conglomerates, which grade to the south (study area) to finer fluvial sandstones, siltstones and claystones of the Solsona Formation (Williams et al., 1998; Barrier et al., 2010).

The Berga and Solsona Formations show growth strata geometries, observed in seismic lines (Vergés, 1993), indicating coeval deposition during the growth of the Puig-reig anticline and emplacement of the Vallfogona thrust (Fig. 2a) (Riba, 1973; Vergés, 1993). The Berga Formation displays outstanding growth strata patterns in the Busa syncline, located between the Puig-reig anticline and the Vallfogona thrust (Riba, 1976; Suppe et al., 1997; Ford et al., 1997) (Fig. 2a).

The study area, along the Cardener River, shows good and continuous exposures of the Berga and mostly Solsona syntectonic formations forming the Puig-reig anticline, cut by a system of faults from which the antithetic normal faults extending its crestal domain are the most prominent.

3. Methodology

3.1. Sampling

The structure of the Puig-reig anticline displays a 10 km long geological cross section (Fig. 2b). To characterize the evolution of the fluids during the formation of this anticline, a structural analysis was combined with the petrographic and geochemical study of 32 polished thin sections made from 26 fracture-filling cements and host rocks (Fig. 4).

3.2. Petrography

Petrographic observations were made using optical and cathodoluminescence microscopy. A CITL Cathodoluminescence device Model 8200 Mk5-1 operating at 13.7 kV and 250 μA gun current was used to distinguish the different cements. Images from thin sections were analysed with the software J-Microvision in order to quantify the host rock components (clasts, cements, porosity). A random point-counting was done, using images of 5 mm^2 for coarse to medium sandstones, 1.5 mm^2 for fine sandstones, 0.5 mm^2 for lutites and 20 mm^2 for palustrine-lacustrine limestones. In addition, point-counting was applied in the matrix of host conglomerates using the same image size areas than in sandstones and lutites, depending on the grain size.

3.3. Fluid inclusions

Fluid inclusions were examined in vein calcite cements to determine composition and temperature conditions of the mineral-forming fluid. Thick sections were used for petrographic characterization of the fluid inclusions and for microthermometric determination. Measurements were made on a Linkam THMS-600 heating-freezing stage.

Raman microspectroscopy analyses were recorded with a LabRam HR800 Jobin-Yvon™ microspectrometer equipped with 600 g/mm gratings and using 785 nm (red) and 532 nm (green) laser excitations. Acquisition timespan was 10 seconds during 10 accumulation spectra.

Vapour bubbles were analysed in order to determine the presence of volatile species (CO_2, CH_4, N_2, H_2S).

3.4. Carbon and oxygen isotopes

Fracture-filling calcite and carbonate host rocks were sampled for carbon- and oxygen-isotope analysis employing a 400 µm-thick dental drill to extract 60 ± 10 µg of powder from trims. The calcite powder was reacted with 100% phosphoric acid for two minutes at 70ºC. The resultant CO_2 was analysed using an automated Kiel Carbonate Device attached to a Thermal Ionization Mass Spectrometer Thermo Electron (Finnigan) MAT-252 following the method of McCrea (1950). The results are precise to ± 0.05‰ for $\delta^{18}O$ and ± 0.01‰ for $\delta^{13}C$ and were corrected using the standard technique (Craig and Gordon, 1965; Claypool et al., 1980), expressed in ‰ with respect to the VPDB (Vienna Pee Dee Belemnite) standard.

3.5. Clumped isotope thermometry

Aliquots (replicates) of carbonate samples weighing 2-3 mg were measured using an automated line for clumped isotopes developed at Imperial College (The IBEX: Imperial Batch EXtraction system). The IBEX is a common acid bath device: individual samples are dropped in 105 % phosphoric acid maintained at 90˚C, and reacted for 30 minutes. The reactant CO_2 is first continuously trapped during the phosphoric acid reaction by freezing it in a trap maintained at liquid nitrogen temperature. Subsequently, water is separated from the gas by heating up the water trap to -100˚C under helium flow, and the gas is then passed through a silver trap to remove sulfur, and through a trap densely packed with Porapak Q held at -35ºC. This has the effect of separating the clean CO_2 gas from potential contaminants, an essential step given that the analyte measured (mass 47 of CO_2) has a natural abundance of only 44 ppm (Eiler, 2007). Lastly, the CO_2 is captured in a second water trap maintained at liquid nitrogen temperature, transferred into a microvolume, and finally transferred into the bellows of the mass spectrometer. Mass spectrometric analyses were performed on a MAT 253 from Thermo

Scientific following analytical protocols first described for the Imperial College lab in Dale et al. (2014), and more generally in Huntington et al. (2009) and Dennis et al. (2011). Full characterization of a replicate consists of 8 acquisitions in dual inlet mode with 7 cycles per acquisition. Each acquisition includes a peak centre, background measurements and an automatic bellows pressure adjustment aimed at a 15V signal at mass 44. The sample gas is measured against an Oztech reference gas standard. Four inter-laboratory carbonate standards from Meckler et al. (2014) were measured to transfer the values into the absolute reference frame (CDES, Dennis et al., 2011), and a fifth standard (Carrara marble) was measured as a sample to ensure data consistency. Correction for non-linearity was performed following the background correction method of Bernasconi et al. (2013). Sample measurements were rejected based on elevated 48 and 49 signals, and the Δ47 values are corrected for isotope fractionation during phosphoric acid digestion using a phosphoric acid correction of 0.069 ‰ at 90°C for calcite following Guo et al. (2009). This value is consistent with a recent empirical evaluation of the phosphoric acid reaction of calcite and aragonite (e.g., Wacker et al., 2013). Carbonate $\delta^{18}O$ values are calculated using the acid fractionation factors of Kim and O'Neil (1997). Each sample was measured at least three times, and the results averaged before being converted to temperatures using the calibration of Kluge et al. (2015).

3.6. Strontium isotopes

For $^{87}Sr/^{86}Sr$ analyses, four samples of 100% calcite from veins, a mudstone and a marly host rock were fully dissolved in 0.5M acetic acid, dried and redissolved in 3M HNO_3. To eliminate the solid residue resulting from reprecipitation after chemical dissolution, samples were centrifuged at 4000 rpm during 10 minutes before being charged in chromatographic columns. Samples were analysed on Re single filament with 1µl of H_3PO_4 1M and 2µl of Ta_2O_5 on a TIMS-Phoenix mass spectrometer. The data acquisition method consists of dynamic multicollection during 10 blocks of 16 cycles each one, with a beam intensity in the ^{88}Sr mass of 3V. Analyses have been corrected for possible interferences of ^{87}Rb. During the analyses, the NBS 987 standard was analysed 5 times obtaining a mean value of 0.710248 and a double standard deviation (STDEV 2σ) of 0.000008. The results were standardized with respect the ^{88}Sr/^{86}Sr value of 0.1194 in order to correct possible mass fractionations during sample analysis. Precision on major element analyses average 0.01% standard error at 2σ confidence levels.

3.7. Elemental composition

Carbon-coated polished thin sections were used to analyse major, minor and trace element concentrations on a CAMECA SX-50 electron microprobe. The microprobe was operated using 20 kV of excitation potential, 15 nA of current intensity and a beam diameter of 10 µm. The detection limits were 140 ppm for Mn, 198 ppm for Fe, 552 ppm for Ca, 128 ppm for Na, 500 ppm for Mg and 430 ppm for Sr. Precision on major element analyses averaged 0.64% standard error at 2σ confidence levels.

4. Structural observations

The studied section of the Puig-reig anticline is deformed by a system of fractures, which includes planar joints perpendicular to bedding and normal and strike-slip faults with displacements smaller than 20 m defining a crestal graben system (Fig. 2b). Few small low-angle thrusts are observed in the forelimb.

Normal faults, observed in the crest of the Puig-reig anticline, are trending NW-SE, oblique to the local fold axis but sub-parallel to the regional trend of the Puig-reig anticline (Fig. 1a). Normal faults dip from 40 to 70 degrees either towards the foreland or the hinterland and intersect bedding at high angle (Fig. 5a). They show displacements from a few centimeters to 15 meters. Kinematic indicators on fault planes show a pure strike-slip or oblique-slip set overprinted by a dip-slip set, pointing to the extensional reactivation of previous strike-slip faults. Fault cores are defined by centimetre-thick discrete planes in normal faults with small displacements and by 2 m-thick gouges and cataclasites along normal faults showing larger displacements. The damage zone is constituted of non-cemented small normal faults and joints.

Dextral and less abundant sinistral strike-slip faults are planar or undulated. They display a high dispersion of trends, dipping from 40 to 90º either towards the foreland and the hinterland, and punctually develop conjugated fault sets (Fig. 5b). Strike-slip faults show high angle relative to bedding, although it is not constant along the studied section. Kinematic indicators on fault planes show a pure strike-slip or extensional oblique-slip motion. Fault cores are few centimetres thick discrete planes filled by calcite or up to 2 m thick fault gouges and cataclasites, whereas damage zones are constituted of small strike-slip faults filled by calcite.

Reverse faults, only observed in the forelimb, are NE-SW trending, nearly sub-perpendicular to the fold axis and are characterized by flat-ramp-flat geometries. Displacements are small, ranging from a few centimetres to 2 m (Fig. 5b). Reverse faults show low angle relative to bedding, regardless of structural position and bedding dip domain. Fault damage zones are not developed whereas discrete planes define fault cores. Slickenlines developed on fault planes indicate in most of cases dip-slip motion. Reverse faults are spatially related to layer-parallel faults, showing both faults detachment horizons at the contact between shales and sandstones.

Joints are stratabound fractures affecting the more competent layers (sandstones and conglomerates) all along the studied section of the Puig-reig anticline.

4.1. <u>Microstructures</u>

The microstructures in the reverse, strike-slip and normal faults zones are similar and consist of calcite shear veins, extension veins and stylolites.

4.1.1. Shear veins

Shear veins are up to 1 centimeter-thick tabular bodies extended along fault planes, bounded by striated shear surfaces and in most cases containing internal, mm-spaced shear surfaces. Shear veins are formed of several millimeter-thick bands of calcite parallel to the vein walls, locally showing rhomb-shaped veinlets separated by host rock bands (Fig. 6a). These veinlets were generated by a crack-seal mechanism and its obliquity with respect shear planes indicates the sense of shear (Ramsay, 1980; Labaume et al., 1991). In addition, sometimes shear veins define S-C patterns with cleavage planes (Fig. 6a). Locally, stylolites parallel to shear planes are present.

4.1.2. Extension veins

The extension veins observed in the studied host rock have been classified in four types according to their shapes, orientations and formation mechanisms: 1) microscopic feather fractures; 2) irregular veins; 3) dilational jogs; and 4) bedding-perpendicular veins. Microscopic feather fractures are formed perpendicular to the cleavage developing S-C structures by shearing (Fig. 6a). They are defined by tapered fractures that are thicker at the contact with shear veins thinning away from the fault. They have been interpreted to form after fault slip (Conrad and Friedman, 1976; Friedman and Logan, 1977; Blenkinsop, 2008). Irregular extension veins exhibit fuzzy contacts with the adjacent host rock (Fig. 6b). Fuzzy contacts may form by alteration of the host rock wall or by deformation and recrystallization of veins with sharp boundaries (Passchier and Trouw, 2005). Dilational jogs are rhomb-shaped veins formed in relay zones between segments of non-cemented shear planes to form vein arrangements (Fig. 6c). Bedding-perpendicular veins are not related to shear planes and punctually show stylolite contacts with clayey host rocks (Fig. 6d). The contact between microscopic feather fractures, dilational jogs and bedding-perpendicular veins and host rock is sharp. Punctually, extension veins show irregular morphologies when are affected by a late stage of shear.

5. Petrology

5.1. Host rock

The Berga and Solsona Formations consist of alluvial and fluvial conglomerates, sandstones and lutites and thin intervals of lacustrine mudstones arranged in thickening and coarsening upward sequences.

Sandstones are stacked in tabular and channelized bodies with grain sizes ranging from fine to coarse. They are formed of mature sublitharenites constituted of 70-80% clasts, 0-5% clay matrix, 10-20% calcite cements and 5% porosity. Sandstones are well-sorted with subrounded clasts made of 80-90% quartz, 10-20% lithic fragments (limestones and metamorphic rocks) and traces of feldspar. In coarse-grained sandstones, some carbonate clasts have undergone ductile deformation to form pseudomatrix.

Conglomerates, which are stacked in channelized bodies, are grey in colour, heterometric, polymictic and present both matrix- and clast-supported fabrics. They are constituted of 50-80% clasts, 10-20% matrix, 10-20% calcite cement and 0-15% porosity. Clasts are rounded, with sizes ranging from 2 mm to 20 cm and consist of lithic fragments mainly derived from Mesozoic and Palaeogene dolostones and limestones in addition to less abundant Palaeozoic granitoids and metamorphic rocks. When clasts of different compositions are in contact, pressure solution processes occur. The matrix is formed by well sorted sandstones (mainly quartz grains) and red lutites.

Lutite layers are composed of red claystones and siltstones. Claystones are constituted of 90-100% of clay minerals and 0-10% of silt grains (mainly subhedral quartz) whereas siltstones are constituted of 50-80% of silt grains and 20-50% of clay minerals.

Carbonates are tabular bodies, up to 0.5 m thick, consisting of palustrine-lacustrine grey-yellow marlstones and brown mudstones. Sometimes they exhibit vug porosities cemented by calcite cement and displaying geopetal structures.

5.2. <u>Host rock and fracture relationships</u>

Point counting indicates that the abundance of fractures highly differs depending on the composition of the host rock (Fig. 7).

Lutite layers characterized by more than 70% of clay matrix are hardly affected by cemented fractures (Fig. 7). However, when the amount of silt increases the fracture porosity raises up to 13-25 % (Fig. 7).

In fine and medium-grained mature sandstones, the intergranular porosity is totally occluded by calcite cement. In such cases, sandstones are not affected by fractures (Fig. 7). In contrast, in coarse-grained sandstones, grains are affected by small fractures, increasing up to a 15% the presence of microfractures filled by calcite cement (Fig. 7).

In conglomerates, the development of fractures differs depending on the fabric. In matrix supported conglomerates, calcite veins are less abundant than in clast supported conglomerates (Fig. 7). These fractures crosscut one or several clasts. The contact between clasts and matrix sometimes is open and filled by calcite cement (Fig. 8a).

Mudstones are slightly affected by fractures (Fig. 7), which locally are interconnected with vug porosities (Fig. 6e and 6f).

5.3. <u>Calcite cements</u>

Two generations of calcite cement have been recognized:

The first generation (Cc1) shows a zoned bright-orange to bright-red luminescence and is observed in the intergranular porosity of the clastic host rocks, vug porosity of host-carbonates and in veins of reverse and most of strike-slip faults. In the intergranular porosity, Cc1 is formed of 5 to 10 µm in size euhedral blocky crystals that partially replace the host rock and previous cementation phases. Evidences of replacement include textures such as: 1) corroded borders of quartz and feldspar grains and protrusions of calcite cement (Fig. 8a and B); 2) pseudomorphs of sand and silt grains (Fig. 8c) and previous fibrous cements (Fig. 8d); and 3) patches of Cc1 microsparite within carbonate-derived conglomerate clasts (Fig. 8e and f). Contrarily, calcite cement Cc1 in veins shows a wider variety of morphologies, such as fibrous, blocky and bladed crystals. Fibrous crystals fill shear veins and change laterally to blocky sparite (Fig. 9a). They are arranged parallel to shear planes indicating a synkinematic growth. The size of fibrous calcite is around 1-1.5 mm long and 100-200 µm thick. Blocky crystals, with growth zonation in punctual cases (Fig. 9b), show differences depending on the type of veins where they precipitated. In shear veins, the size of blocky crystals ranges from 100 to 500 µm whereas in extension veins the size is smaller (from 5 to 10 µm). Bladed crystals, with widths and lengths up to 100 µm and 300 µm respectively, are developed in the margins of all vein types.

The second generation of calcite cement (Cc2) shows a zoned dull-orange to dull-red luminescence and it has been only observed in shear veins of all normal and some strike-slip faults. It consists of blocky crystals with sizes ranging from 100 µm to 5 mm.

The contact between Cc1 and Cc2 calcite cements within shear veins is sharp (Fig. 9c and d) or gradual (Fig. 9e and f). Moreover, all the cement textures in veins and the intergranular porosity show mechanical twinning, subgrain formation and serrated borders.

6. Fluid inclusion analysis

Fluid inclusions trapped in calcite cements have been studied by optical microscope and Raman spectroscopy.

Primary and secondary fluid inclusions have been observed in both calcite cement generations. However, their irregular shape and variable vapour/liquid ratios indicate that they were stretched as it is also attested by the wide range of temperatures of homogenization (between 130 to 210°C for Cc1 and 120 to 280°C for Cc2) (Fig. 10). Therefore, these fluid inclusions are unusable for microthermometry analysis. In addition, the salinity of the fluid could not be determined since the obtained elevated ice melting temperatures indicate the presence of clathrates (Goldstein and Reynolds, 1994), which hide the final disappearance of ice during melting (Diamond, 1994). It has not been possible to determine the eutectic temperature in this case. Raman spectroscopy was also applied in fluid inclusions trapped in calcite cements Cc1 and Cc2. However, in all samples, the strong fluorescence of calcite crystals did not allow to analyse their liquid and vapour phases.

7. Geochemistry

7.1. Carbon and oxygen isotopes

Within the host rock, carbonate clasts of conglomerates show $\delta^{13}C$ values between -3.22 and +3.11‰ VPDB and $\delta^{18}O$ values between -8.91 and -3.43‰ VPDB (Fig. 11; Table 1). Palustrine-lacustrine limestones show $\delta^{13}C$ values between -3.3 and -2.4‰ VPDB and $\delta^{18}O$ values between -7.28 and -6.91‰ VPDB (Fig. 11; Table 1). These values are within the range of carbonates precipitated in lakes fed by rivers of Pyrenean provenance (Oberhänsli and Allen, 1987).

Calcite cement Cc1 shows $\delta^{13}C$ values between -2.5 and +1 ‰ VPDB and $\delta^{18}O$ values between -9 and -6 ‰ VPDB (Fig. 11, Table 1). Calcite cement Cc2, shows $\delta^{13}C$ values between -2 and +0.5‰ VPDB and $\delta^{18}O$ values between -14 and -9.5‰ VPDB (Fig. 11, Table 1).

7.2. <u>Clumped isotope thermometry</u>

For calcite cement Cc1, the measured Δ_{47} values by clumped isotope geochemistry are 0.548 ± 0.009 ‰ and 0.493 ± 0.0010 ‰, which translates into temperatures of 92 ± 5°C and 129 ± 8°C using the form of Kluge et al. (2015) (Table 2). In addition, the $\delta^{18}O_{fluid}$ composition for calcite cement Cc1 can be reconstructed using the clumped isotope temperatures, the $\delta^{18}O_{calcite}$ and the equation of Friedman and O'Neil (1977). Thus, the $\delta^{18}O_{fluid}$ for Cc1 is estimated to range between +4.7 ± 0.6 and +9.2 ± 0.7‰ VSMOW.

The measured Δ_{47} values for calcite cement Cc2 are 0.574 ± 0.010 ‰ and 0.551 ± 0.004 ‰, which translate to temperatures of 77 ± 5°C and 93 ± 1°C using the calibration of Kluge et al. (2015) (Table 2). The estimated $\delta^{18}O_{fluid}$ for calcite cement Cc2 ranges between -1.7 ± 0.7 and -0.7 ± 0.3‰ VSMOW.

7.3. <u>Strontium isotopes</u>

The host mudstone has a $^{87}Sr/^{86}Sr$ ratio of 0.708865 and the calcite fraction of the marls has a $^{87}Sr/^{86}Sr$ ratio of 0.708967 (Fig. 12; Table 3).

$^{87}Sr/^{86}Sr$ ratios for calcite cement Cc1 range between 0.709138 and 0.709246 and between 0.708947 and 0.709002 for calcite cement Cc2 (Fig. 12, Table 3).

7.4. <u>Elemental composition</u>

The elemental composition of calcite cement Cc1 (Fig. 13, Table 4) show values ranging from 600 to 4500 ppm in Mg and from 600 to 2800 ppm in Mn. Fe and Sr contents range from below the detection limit up to 3100 and up to 700 ppm, respectively.

Calcite cement Cc2 (Fig. 13, Table 4) show values from 300 to 2300 ppm in Mn and from 300 to 3200 ppm in Fe. Mg and Sr contents range from below detection limit up to 2400 and 3000 ppm, respectively.

8. Discussion

Discussion is organized in 5 main subsections discussing 1) the mechanical stratigraphy; 2) the type and origin of fluids across the Puig-reig anticline; 3) the mechanisms of calcite cement precipitation; 4) the relationships between fluid flow and the structural evolution of the Puig-reig anticline and 5) the evolution of fluid flow at the basin scale comparing the Puig-reig anticline results with the El Guix anticline (~32 km southwards), which is located along the SE Pyrenean deformation front within the Ebro basin.

8.1. Mechanical stratigraphy

Cementation during early burial mostly affected sandstone and conglomerate layers due to their higher porosity and permeability than clayey units. This early cementation, however, increased the relative mechanical strength of these layers and thus localizing the generation of stratabound joints across the entire anticline as described in other deformed basins (David et al., 1998; Shackleton et al., 2005; Laubach et al., 2009). Differences in rock mechanics between layers also controlled the development of bed-parallel slip surfaces and associated reverse faults in the forelimb of the Puig-reig anticline during compression, as was also observed in other thrust belts (Treagus, 1988; Bai and Pollard, 2000; Sanz et al., 2008).

Joints were reactivated as strike-slip and normal faults by shearing as evidenced by the high angle dips with respect to bedding and the stratabound character of some faults (like joints). Some of these faults crosscut competent and non-competent layers and they are mainly located in the crest and forelimb of the Puig-reig anticline. Thus, at outcrop scale, fracture patterns in the Puig-reig anticline were controlled by tectonic stress related to contraction, rock mechanics, diagenesis and structural position within the anticline. These controls on fracturation have been also observed in other foreland fold belts (Shackleton et al., 2005; Laubach et al., 2009; Watkins et al., 2015).

At microscopic scale, the development of microstructures was controlled by grain size, host rock cementation and porosity. In fine to medium-grained sandstones and matrix-supported conglomerates, fractures are absent, whereas in coarse-grained sandstones and clast-supported conglomerates, grain crushing increases up to 15 % and 8 %, respectively (Fig. 7). In conglomerates in which carbonate and silicic clasts are in contact, stylolite contacts are developed instead of fractures. Intergranular porosity of all these sediments was occluded by calcite cement Cc1 indicating that cementation together with grain size exerted a strong control on fracture development. In this study, coarse-grained rocks are more prone to fracturing than finer rocks, as was also observed from experimental tests by Chuhan et al. (2002) in sandstones, reporting an increase of grain crushing during compaction related with an increase of grain size. In fine lutite units (claystone) and conglomerates supported by clay matrix fractures are hardly present (Fig. 7) because the absence of cements makes them to behave as ductile levels when are affected by deformation. Siltstone layers were more permeable, and are partially cemented, increasing their stiffness and facilitating brittle deformation. Therefore, development of fractures in lutite layers was controlled by cementation, which changed rock mechanics (Laubach et al., 2009). Fractures in palustrine-lacustrine mudstones were controlled by vug porosity (Fig. 6e and 6f), which probably facilitated fracture nucleation (Vajdova et al., 2010).

8.2. <u>Type and origin of the fluids</u>

The type of fluid that flowed through the intergranular porosity of host rocks and fault planes has been determined by using the isotopic and elemental composition of the carbonate cements (Meyers and Lohmann, 1985; Banner and Hanson, 1990).

8.2.1. Cement Cc1

Calcite cement Cc1, precipitated in the intergranular porosity, reverse and most of strike-slip faults. The temperatures from which cement Cc1 precipitated (between 92^{o}C and 129^{o}C) would imply burial depths between 4 and 5 km, assuming a geothermal gradient of 25^{o}C km^{-1}.

These depths have never been attained according to previous works based on cross sections (Vergés, 1993), stratigraphic profiles (Barrier et al., 2010) and vitrinite reflectance data (Clavell, 1992; Vergés et al., 1998), which indicate a maximum depth of 1.7 km for the Solsona Formation in the Puig-reig anticline. Thus, with a thickness of 1.7 km and a geothermal gradient of 25ºC km^{-1}, the temperature reached at the base of the Solsona Formation was around 42ºC, which is lower than that obtained from clumped isotopes. These results account for the occurrence of hydrothermal fluids circulating channelized along the thrust faults from the Palaeozoic basement at depths of around 4-5 km upwards to the shallower Solsona Formation (Fig. 2a). This hydrothermal fluid should have flowed rapid enough to be at thermal disequilibrium with its adjacent host rock (Beaudoin et al., 2011).

Calcite cement Cc1 is characterized by a narrow range of $\delta^{18}O$ (from -7.53 to -5.93‰ VPDB) and $\delta^{13}C$ within the same range of the host carbonates (Fig. 11), probably a result of the buffering of the pore-water isotopic composition by the host carbonates (Marshall, 1992; Travé et al., 1998b; Fig. 14). $\delta^{18}O$ of strike-slip faults have a wider range of values (from -9.63 to -6.25‰ VPDB), with some veins in disequilibrium with their host carbonates (Fig. 14).

The calculated $\delta^{18}O_{fluid}$ from clumped isotope thermometry (Table 3) range between +4.7 and +9.2 ‰ VSMOW, within the range of formation, metamorphic and magmatic waters (Taylor, 1987). Magmatic waters are ruled out since magmatism is not developed during the formation of the Pyrenees. However, we have no evidences to discern between formation and metamorphic waters. The high $^{87}Sr/^{86}Sr$ values (between 0.709138 and 0.709246) indicate that the hydrothermal fluid interacted with a highly radiogenic source (Fig. 12, Table 2). The source for this highly radiogenic fluid can be the Palaeozoic basement located at depth and/or the Palaeozoic-derived silicic clasts of the Solsona and Berga Formations. The $^{87}Sr/^{86}Sr$ of Pyrenean Palaeozoic sedimentary rocks range between 0.709600 and 0.717000 and between 0.706633 and 0.715405 for granitic rocks (Bickle et al., 1988; Banks et al., 1991). The low radiogenic underlying evaporite units of the Cardona (between 0.70798 and 0.70800), Barbastro (0.70796) and Beuda (between 0.707739 and 0.707980) Formations (Travé et al., 2000; Carrillo, 2012; Carrillo et al., 2014), do not seem to be involved. The $\delta^{18}O$ of the Palaeozoic metamorphic rocks in the Pyrenees (between +10 and +16 ‰ VSMOW; Wickham and Taylor, 1985, 1987) and Hercynian granodiorites (up to +9 ‰ VSMOW; Wickham and Taylor, 1987; Losh, 1989; Tempest, 1991) is also consistent with a fluid highly interacted with the Palaeozoic basement.

8.2.2. Cement Cc2

The $\delta^{13}C$ of cement Cc2 is similar to that of cement Cc1 (Fig. 11). However, the $\delta^{18}O$ relationship between calcite cement and host rock indicates that the fluid from which Cc2 precipitated was not in equilibrium with its adjacent host carbonates (Fig. 14). The depletion in $\delta^{18}O$ of Cc2 with respect to Cc1 is interpreted as the progressive input of a meteoric external fluid (Travé et al., 1997), more evident in the crest of the anticline (Fig. 15). The lower $^{87}Sr/^{86}Sr$ of cement Cc2 with respect to Cc1 (Fig. 12) indicates not interaction of the fluid with a radiogenic source.

The $\delta^{18}O_{fluid}$ obtained from clumped isotopes (Table 3), between -1.7 ‰ and -0.7 ‰ VSMOW, are higher than those of modern rainfall in the same area (from -6.4 to -4.6‰ VSMOW; Travé and Calvet, 2001) and probably also of the upper Eocene and lower Oligocene rainwater, taking into account that during this time the Iberian plate was in similar latitude than present day (Rosenbaum et al., 2002). These values may result from mixing of meteoric waters with a more $\delta^{18}O$-enriched fluid. The wide range of $\delta^{18}O$ (Fig. 11), low Mg and Mn content and high Fe and Sr content (Fig. 13), also account for a mixing between fluids.

Temperatures obtained for calcite cement Cc2 (between 77ºC and 93ºC), although lower than those obtained for Cc1, they still account for hydrothermal fluid flow, taking into account the minimum burial depth of 1.7 km and assuming a geothermal gradient of 25ºC km^{-1}. This temperature decrease would also agree with Cc2 precipitation from the mixing between the hydrothermal fluid responsible of Cc1 precipitation and a low temperature meteoric fluid.

The increase in Fe and Sr content in cement Cc2 compared to Cc1 could be controlled by the progressive burial and compaction of shale units of the Solsona Formation, leading to ion expulsion from shales (Coplen and Hanshaw, 1973; Hanshaw and Coplen, 1973; Travé et al., 1997) and increasing the Fe content towards the deeper stratigraphic levels (Fig. 15).

8.3. Mechanisms of calcite cement precipitation

Calcite cements Cc1 and Cc2 are in thermal disequilibrium with the surrounding host rock. However, since calcite has a retrograde solubility, and preferentially precipitates when temperature increases, other parameters have to take into account when calcite precipitates from a hot ascending fluid (Segnit et al., 1962; Fein and Walther, 1987). According to Bons et al. (2012) and Beaudoin et al. (2014), controlling parameters such as changes in pH and in oxidation conditions as well as fluid mixing influence the Ca oversaturation of the fluid, which can promote precipitation of calcite cement, even when fluids are decreasing their temperature. Another controlling parameter is the decrease in pCO_2 during fracture opening. Moreover, during faulting, zones of low pCO_2 are developed, allowing fluid migration into fractures and precipitation of calcite cements Cc1 and Cc2 (Bons et al., 2012).

If calcite cement precipitation was coeval with fracture opening (as evidenced by veins with elongated blocky calcite), the $\delta^{18}O$ composition allows us to determine which specific parameters controlled calcite precipitation (Beaudoin et al., 2014). Thus, the narrow range of $\delta^{18}O$ values for calcite cement Cc1 present in the intergranular porosity and reverse and some strike-slip faults indicates that precipitation was controlled by pCO_2 drop related to fracturing. In contrast, the wide range in $\delta^{18}O$ in calcite cement Cc1 and Cc2 present in some strike-slip and in all normal faults may be indicative that the main controlling parameter of calcite precipitation was mixing of two fluids.

8.4. <u>Relationship between fluid flow and structural evolution of the Puig-reig anticline</u>

In the Puig-reig anticline, calcite cements Cc1 and Cc2 are related to two fluid flow stages during fold growth. Cement Cc1 is related to layer-parallel shortening whereas cement Cc2 relates to the fold growth. Earlier cements precipitated before the growth of the anticline and are totally replaced by calcite cement Cc1 (Fig. 8).

8.4.1. Fluid flow during layer-parallel shortening (time T1)

Relationships between fractures and calcite cement Cc1 in the Puig-reig anticline indicate precipitation during layer-parallel shortening as evidenced by the constant angular relations between reverse and most of the strike-slip faults with bedding (Fig. 16). The same relationships between bedding and fractures during layer-parallel shortening have been also observed in anticlines formed in the Zagros fold and thrust belt (Casini et al., 2011; Reif et al., 2012; Tavani et al., 2015). Reverse faults in the forelimb and strike-slip faults in the hinge of the Puig-reig anticline could have been formed due to an increase of fluid pressure, controlled by fluid migration to the fold crest and/or by syntectonic sedimentation, as pointed out in other fold-fluid systems (Evans and Fischer, 2012).

During T1, hydrothermal fluids migrated upwards, using faults as preferential paths. This fluid migrated along the blind thrust system responsible for the development of the Puig-reig anticline reaching the overlying Solsona and Berga Formations through the reverse and strike-slip fault planes affecting these units (Figs. 16 and 17). These fractures allowed hydrothermal fluid circulation, cementing the permeable layers in the system (sandstones, conglomerate sand matrix and siltstones) and replacing earlier cements. Although the studied reverse and strike-slip faults are relatively small, they probably form a well-connected network allowing lateral and vertical fluid migration across different stratigraphic units, as already observed in the Bighorn Basin (Beaudoin et al., 2013).

8.4.2. Fluid flow during fold growth (time T2)

During the second stage of fluid flow, cement Cc2 precipitated (Fig. 16). Normal faults, which are sub-parallel to the regional fold axis, were formed due to the outer-arc extension of the Puig-reig anticline during fold growth. In addition, during T2, previous faults and bedding-perpendicular joints were passively rotated into the limbs and suitably oriented strike-slip faults were reactivated as normal faults, as observed by the presence of dip-slip striae overprinting strike-slip markers in the same fault planes.

Cement Cc2 is only present in fault planes due to the entire cementation of the more permeable units by cement Cc1 during T1. Small normal and strike-slip faults formed during T2 developed sufficient vertical connectivity to allow vertical fluid flow across the previously cemented sedimentary units. The newly formed normal and strike-slip faults changed the palaeohydrological system acting as paths for low-temperature, probably meteoric, fluids (Fig. 16). These fluids reached the interface between the Solsona and Igualada Formations in the core of the Puig-reig anticline (Fig. 17), in accordance with the fault-valve model (Sibson, 1981; Henderson and McCaig, 1996). According to this model, fluids migrate downwards through short-displacement faults by decrease in fluid pressure (P_f) at depth after the seismogenic cycle of an underlying thrust fault (Fig. 17). The low-temperature fluids were enriched at depth in Fe and Sr and mixed with the hydrothermal fluid from which cement Cc1 precipitated, according to the model of Bons et al. (2014). After mixing, fluids migrated upwards through normal and strike-slip faults (precipitating cement Cc2 by pCO_2 drop) due to an increase of P_f related to the build-up stresses developed during compression, as described in the central Pyrenees (Henderson and McCaig, 1996).

This evolution of the fluid flow model is consistent with previous works done in fold-fluid systems, reporting the opening of the fluid system to external fluids and mixing during development of fold-related fractures (Travé et al., 2000; Fischer et al., 2009; Beaudoin et al., 2011; Evans et al., 2012; Ogata et al., 2014).

8.5. <u>Fluid flow at basin scale</u>

8.5.1. The El Guix anticline

The El Guix anticline developed at the southern tip line of the South Pyrenean fold and thrust belt during the lower Oligocene (Sans and Vergés, 1995). This anticline is detached above the Cardona salt, which is the main detachment level between the deformed and non-deformed foreland basin (Figs. 1b and 2a). The El Guix anticline has a long wavelength (5.6 km), small amplitude and consists of two anticlines at the present erosion level (Sans, 2003). The sedimentary cover forming the El Guix anticline consists of the distal part of the Solsona Formation, the deltaic-lacustrine units of the Súria and Torà formations and the Barbastro gypsum (Travé et al., 2000). These sediments are located 300 m above the Cardona detachment horizon and are affected by a set of thrusts and backthrusts with dips ranging from 27 to 40^{o} (Sans and Vergés, 1995).

8.5.2. Puig-reig anticline vs El Guix anticline

In the El Guix anticline, three fluid flow stages were established, whereas in the Puig-reig anticline only 2 fluid flow stages have been determined in this study.

The first fluid flow stage of the El Guix anticline was characterized by local migration of meteoric waters through microfractures developed by layer-parallel shortening in a relatively open system. In the Puig-reig anticline this stage has not been observed. However, the presence of early cements replaced by calcite cement Cc1 indicates the presence of a previous fluid flow stage.

The second fluid flow stage of the El Guix anticline took place during the folding and thrusting. During these events, external meteoric fluids flowed downwards to the detachment horizon located in the Cardona Formation and through the main backthrusts, which acted as effective channelized paths for these fluids (Travé et al., 2000). During their migration, these meteoric waters evolved to a formation water composition. In contrast, in the Puig-reig anticline, hydrothermal fluids circulated along the basal thrust of the South Pyrenean thrust system (Figs. 2a and 17). These hydrothermal fluids were mixed at depth with meteoric waters that percolated downwards through normal and strike-slip faults. Cement Cc2 precipitated when the mixed fluids migrated upwards during compression. The lack of such cements in the El Guix anticline reveals that hydrothermal fluids did not reach the frontal most part of the fold and thrust system, indicating that these fluids were probably diluted during their forward migration, as has been already pointed in other fold and thrust belts such as the Bighorn Basin (Beaudoin et al., 2014).

Formation waters in the El Guix anticline and hydrothermal fluids in the Puig-reig anticline circulated in a rock-buffered system, as evidenced by the $\delta^{13}C$ signal of calcite cements and carbonate host rocks. In both structures, fluids interacted with the upper Eocene-lower Oligocene lacustrine mudstones and marlstones (between -5.6 and -3.71 ‰ VPDB in the El Guix anticline and between -3.3 and -2.4‰ VPDB in the Puig-reig anticline). In addition, in the Puig-reig anticline, hydrothermal fluids also interacted with conglomerate clasts derived from Jurassic, Cretaceous and Paleogene marine carbonates (between -3.22 and +3.11‰ VPDB).

The last fluid flow stage of the El Guix anticline was interpreted to have developed during the extensional elastic rebound of the south eastern margin of the Ebro basin during the opening of the Valencia Trough in late Oligocene-early Miocene times (Lewis et al., 1996). During this extensional stage, local meteoric fluids flowed through fractures and through vug porosity developed within the cement of previous microstructures (Travé et al., 2000).

8.5.3. Migration paths

As discussed previously, hydrothermal fluids are only recognised in the Puig-reig anticline and not in the El Guix anticline. Two possible origins are pointed for these hydrothermal fluids: formation waters or metamorphic fluids. In both cases, large thrust faults would have acted as channelled paths for fluids that migrated from the inner part of the Pyrenees towards the thrust front, as was also stated in the Ainsa basin (Travé et al., 1997).

Later, low temperature meteoric waters were introduced into the palaeohydrological system in the frontal part of the South Pyrenean fold and thrust belt. In the El Guix anticline, local meteoric fluids, which evolved to formation waters, migrated downwards by lateral variations of the topography to the detachment level in the Cardona salts (Travé et al., 2000), whereas in the Puig-reig anticline, fluids percolated to deeper parts of this fold through the crestal graben fracture system reaching the Solsona-Igualada interface and the blind thrust system that created the anticline.

9. Conclusions

A multidisciplinary approach has been used in this study to determine controls on deformation and fluid interactions within a fault system (normal and strike-slip faults) cutting Eocene-Oligocene alluvial and fluvial deposits of the Berga and Solsona Formations, along the crestal domain of the Puig-reig anticline in the SE Pyrenees.

Structural analyses indicate the timing of fracture development, which consists first in the development of joints, small reverse and strike-slip faults and the later extensional reactivation of suitably oriented strike-slip faults as normal faults. At outcrop scale, development of these fractures was controlled by rigidity contrasts between layers, diagenesis and structural position within the anticline, whereas grain size, cementation and porosity controlled deformation at microscopic scale.

Structural, petrographic and geochemical data from intergranular cements and calcite veins reveal the presence of two migrating fluids producing two cementation events: Cc1 related to the layer-parallel shortening and Cc2 linked to the anticline growth.

Cc1 cement precipitated from an ascending hydrothermal fluid at temperatures between 92 and 130ºC. This fluid had $\delta^{18}O_{fluid}$ between +4.7 and +9.2 ‰ VSMOW, relatively high $^{87}Sr/^{86}Sr$ ratio, and high Mn and Mg content and relatively low Sr and Fe content. This fluid was probably a result of the buffering of the pore-water isotopic composition by the host carbonates. Hydrothermal fluids migrated from around 4-5 km depth through the fracture system, including most of the strike-slip faults, to reach the Berga and Solsona Formations, during the layer-parallel shortening, partially replacing the host rocks by calcite. Cc1 precipitation was induced by pCO2 drop related to fracturing.

Cc2 cement precipitated from a fluid in disequilibrium with its adjacent host rock at a temperature between 77 and 93ºC. This fluid, with $\delta^{18}O_{fluid}$ between -1.7 ‰ and -0.7 ‰ VSMOW, relatively low $^{87}Sr/^{86}Sr$ and Mg, and high Sr and Fe content, resulted from the mixing at depth of the hydrothermal fluid from which Cc1 precipitated and low-temperature, probably meteoric, waters. Low-temperature fluids percolated through the crestal graben fault system according to the fault-valve model during the growth of the Puig-reig anticline.

Fluid flow patterns between the Puig-reig and the El Guix anticlines along the same transect reveal that hydrothermal fluids migrated from N to S but did not reach the El Guix anticline along the tip line of the South Pyrenean fold and thrust belt. In this anticline, local meteoric and evolved meteoric fluids circulated along the fold.

Hydrothermal fluids derived from the inner part of the Pyrenean Chain migrated forelandwards, whereas meteoric fluids in the Puig-reig and the El Guix anticlines were added into the fluid system along the frontal parts of the evolving Ebro foreland fold and thrust belt.

Acknowledgements

The Isotopic, Raman and electron microprobe analyses were carried out at "Centres Científics i Tecnològics" of the Universitat de Barcelona. Strontium analyses were done at the "CAI de Geocronología y Geoquímica Isotopica (UCM-CEI)" of the Universidad Complutense de Madrid. Fluid inclusion thermometry was performed at the facilities of the "Departament de Geologia" of the Universitat Autònoma de Barcelona. The clumped isotopes analyses were performed in the Qatar Stable Isotope Laboratory of Imperial College of London. We thank Mercè Corbella, Esteve Cardellach and Dídac Navarro for their support during fluid inclusion analysis. This research was performed within the framework of DGICYT Spanish Project CGL2015-66335-C2-1-R, Grup Consolidat de Recerca "Geologia Sedimentària" (2014SGR-251). The accurate and constructive comments from two anonymous reviewers and from the guest editor O. Lacombe helped to improve the original manuscript.

References

Bai, T., Pollard, D.D., 2000. Fracture spacing in layered rocks: a new explanation based on the stress transition. Journal of Structural Geology 22, 43-57.

Banks, D.A., Davies, G.R., Yardley, B.W.D., McCaig, A.M., Grant, N.T., 1991. The chemistry of brines from an Alpine thrust system in the Central Pyrenees: An application of fluid inclusion analysis to the study of fluid behavior in orogenesis. Geochimia et Cosmochimica Acta 55, 1021-1030.

Banner, J.L., Hanson, G.N., 1990. Calculation of simultaneous isotopic and trace element variations during water-rock interaction with applications to carbonate diagenesis. Geochimia et Cosmochimica Acta 54, 3123-3137.

Barbier, M., Leprêtre, R., Callot, J.P., Gasparrini, M., Daniel, J.M., Hamon, Y., Lacombe, O., Floquet, M., 2012. Impact of fracture stratigraphy on the paleo-hydrogeology of the Madison Limestone in two basement-involved folds in the Bighorn basin, (Wyoming, USA). Tectonophysics 576-577, 116-132.

Barrier, L., Proust, J.N., Nalpas, T., Robin, C., Guillocheau, F., 2010. Control of alluvial sedimentation at foreland basin active margins, case study from the north-eastern Ebro basin (south-eastern Pyrenees, Spain). Journal of Sedimentary Research 80, 728-749.

Beaudoin, N., Bellahsen, N., Lacombe, O., Emmanuel, L., 2011. Fracture-controlled paleohydrogeology in a basement-cored, fault-related fold: Sheep Mountain Anticline, Wyoming, United States. Geochemistry, Geophysics, Geosystems 12, 1-15.

Beaudoin, N., Lacombe, O., Bellahsen, N., Emmanuel, L., 2013. Contribution of Studies of Sub-Seismic Fracture Populations to Paleo-Hydrological Reconstructions (Bighorn Basin, USA). Procedia Earth and Planetary Science 7, 57-60.

Beaudoin, N., Bellahsen, N., Lacombe, O., Emmanuel, L., Pironon, J., 2014. Crustal-scale fluid flow during the tectonic evolution of the Bighorn Basin (Wyoming, USA). Basin Research 26, 403-435.

Beaudoin, N., Huyghe, D., Bellahsen, N., Lacombe, O., Emmanuel, L., Mouthereau, F., Ouanhnon, L., 2015. Fluid systems and fracture development during syn-depositional fold growth: An example from the Pico del Aguila anticline, Sierras Exteriores, southern Pyrenees, Spain. Journal of Structural Geology 70, 23-38.

Bergman, S.C., Huntington, K.W., Crider, J.G., 2013. Tracing paleofluid sources using clumped isotope thermometry of diagenetic cements Along the Moab Fault, Utah. American Journal of Science 313, 490-515.

Bernasconi, S.M., Hu, B., Wacker, U., Fiebig, J., Breitenbach, S.F.M., Rutz, T., 2013. Background effects on Faraday collectors in gas-source mass spectrometry and implications for clumped isotope measurements. Rapid Communications in Mass Spectrometry 27, 603-612.

Bickle, M.J., Wickham, S.M., Chapman, H.J., Taylor, H.P., 1988. A strontium, neodynium and oxygen study of hydrothermal metamorphism and crustal anatexis in the Trois Seignerus Massif, Pyrenees, France. Contributions to Mineralogy and Petrology 100, 399-417.

Bitzer, K., Travé, A., Carmona, J.M., 2001. Fluid flow processes at basin scale. Acta Geologica Hispanica 36, 1-20.

Blenkinsop, T.G., 2008. Relationships between faults, extension fractures and veins, and stress. Journal of Structural Geology 30, 622-632.

Bons, P.D., Elburg, M.A., Gómez-Rivas, E., 2012. A review of the formation of tectonic veins and their microstructures. Journal of Structural Geology 43, 33-62.

Bons, P.D., Fusswinkel, T., Gómez-Rivas, E., Markl, G., Wagner, T., Walter, B., 2014. Fluid mixig from below in unconformity-related hydrothermal ore deposits. Geology 42, 1035-1038.

Burbank, D.W., Puigdefàbregas, C., Muñoz, J.A., 1992a. The chronology of the Eocene tectonic and stratigraphic development of the Eastern Pyrenean Foreland Basin. NE Spain. Geol. Soc. America Bull. 104, 1101-1120.

Burbank, D.W., Vergés, J., Muñoz, J.A., Bentham, P., 1992b. Coeval hinward- and forward-imbricating thrusting in the south-central Pyrenees, Spain: Timing and rates of shortening and deposition. Geological Society of America Bulletin 104, 3-17.

Caja, M.A., Permanyer, A., Marfil, R., Al-Asm, I.S., Martín-Crespo, T., 2006. Fluid flow record from fracture-fill calcite in the Eocene limestones from the South-Pyrenean Basin (NE Spain) and its relationship to oil shows. Journal of Geochemical Exploration 89, 27-32.

Carrillo, E., 2012. The Evaporites of the Southeastern Pyrenean Basin (Late Cuisian – Lutetian): Sedimentology and Structure. PhD Thesis, University of Barcelona, Barcelona, Spain, p. 192.

Carrillo, E., Rosell, L., Ortí, F., 2014. Multiepisodic evaporite sedimentation as an indicator of palaeogeographical evolution in foreland basins (South-eastern Pyrenean basin, Early–Middle Eocene. Sedimentology 61, 2086-2112.

Casini, G., Gillespie, P.A., Vergés, J., Romaire, I., Fernández, N., Casciello, E., Saura, E., Mehl, C., Homke, S., Embry, J.-C., Aghajari, L., Hunt, D.W., 2011. Sub-seismic fractures in Foreland fold and Thrust belts: insight from the Lurestan Province, Zagros Mountains, Iran. Petroleum Geoscience 17, 263-282.

Clavell, E., 1992. Geologia del petroli de les conques terciàries de Catalunya. PhD thesis, University of Barcelona, p. 488.

Claypool, G.E., Kaplan, W.T., Kaplan, I.R., Sakai, H., Zak, I., 1980. The age curves of sulfur and oxygen isotopes in marine sulfate and their mutual interpretations. Chemical Geology 28, 199-260.

Conrad, R.E., Friedman, M., 1976. Microscopic feather fractures in the faulting process. Tectonophysics 33, 187-198.

Conti, S., Fontana, D., Mecozzi, S., Panieri, G., Pini, G.A., 2010. Late Miocene seep-carbonates and fluid migration on top of the Montepetra intrabasinal high (Northern Apennines, Italy): Relations with synsedimentary folding. Sedimentary Geology 231, 41-54.

Coplen, T.B., Hanshaw, B.B., 1973. Ultratitration by a compacted clay membrane-I. Oxygen and hydrogen isotopic fractionation. Geochimia et Cosmochimica Acta 37, 2295-2310.

Costa, E., Garcés, M., López-Blanco, M., Beamud, E., Gómez-Paccard, M., Larrasoaña, J.C., 2010. Closing and continentalization of the South Pyrenean foreland basin (NE Spain): magnetochronological constraints. Basin Research 22, 904-917.

Craig, H., Gordon, I. I., 1965. Deuterium and oxygen-18 variations in the ocean and the marine atmosphere, in: Tongiorgi, E. (Ed.), Proceedings of a Conference on Stable Isotopes in Oceanographic Studies and Paleotemperatures. Consiglio Nazionale delle Richerche, Laboratorio di Geologia Nucleare, Pisa, Italy, pp. 9-130.

Chandonais, D.R., Onasch, C.M., 2014. Fluid history of the Blue Ridge anticlinorium in the central Appalachians. Journal of Structural Geology 69, 415-427.

Choukroune, P., team, E., 1989. The ECORS Pyrenean deep seismic profile reflection data and the overall structure of an orogenic belt. Tectonics 8, 23-39.

Chuhan, F., Kjeldstad, A., BjØrlykke, K., HØeg, K., 2002. Porosity loss in sand by grain crushing - experimental evidence and relevance to reservoir quality. Marine and Petroleum Geology 19, 39-53.

Dale, A., John, C.M., Mozley, P.S., Smalley, P.C., Muggeridge, A.H., 2014. Time-capsule concretions: Unlocking burial diagenetic processes in the Mancos Shale using carbonate clumped isotopes. Earth and Planetary Science Letters 394, 30-37.

David, C., Menendez, B., Bernabe, Y., 1998. The mechanical behavior of synthetic sandstone with varying brittle cement content. International Journal of Rock Mechanics and Mining Sciences and Geomechanics Abstracts 35, 759-770.

Dennis, K.J., Affeck, H.P., Passey, B.H., Schrag, D.P., Eiler, J.M., 2011. Defining an absolute reference frame for ‘clumped’ isotope studies of CO2. Geochimia et Cosmochimica Acta 75, 7117-7131.

Dewaele, D., Muchez, P., Banks, D.A., 2004. Fluid evolution along multistage composite fault systems at the southern margin of the Lower Palaeozoic Anglo-Brabant fold belt, Belgium. Geofluids 4, 341-356.

Dewever, B., Swennen, R., Breesch, L., 2013. Fluid flow compartmentalization in the Sicilian fold and thrust belt: Implications for the regional aqueous fluid flow and oil migration history. Tectonophysics 591, 194-209.

Diamond, L.W., 1994. Salinity of multivolatile fluid inclusions determined from clathrate hydrate stability. Geochimia et Cosmochimica Acta 58, 19-41.

Dromgoole, E.L., Walter, L.M., 1990. Iron and manganese incorporation into calcite: effects of growth kinetics, temperature, and solution chemistry. Chemical Geology 81, 311-336.

Eiler, J.M., 2007. "Clumped-isotope" geochemistry—The study of naturally-occurring, multiply-substituted isotopologues. Earth and Planetary Science Letters 262, 309-327.

Evans, M.A., Bebeout, G.E., Brown, C.H., 2012. Changing fluid conditions during folding: An example from the central Appalachians. Tectonophysics 576-577, 99-115.

Evans, M.A., Fischer, M.P., 2012. On the distribution of fluids in folds: A review of controlling factors and processes. Journal of Structural Geology 44, 2-24.

Fein, J.B., Walther, J.V., 1987. Calcite solubility in supercritical CO2-H2O fluids. Geochimia et Cosmochimica Acta 51, 1665-1673.

Ferket, H., Swennen, R., Arzate, S.O., Roure, F., 2006. Fluid flow evolution in petroleum reservoirs with a complex diagenetic history: An example from Veracruz, Mexico. Journal of Geochemical Exploration 89, 108-111.

Fischer, M.P., Higuera-Díaz, I.C., Evans, M.A., Perry, E.C., Lefticariu, L., 2009. Fracture-controlled paleohydrology in a map-scale detachment fold: Insights from the analysis of fluid inclusions in calcite and quartz veins. Journal of Structural Geology 31, 1490-1510.

Ford, M., Williams, E.A., Artoni, A., Vergés, J., Hardy, S., 1997. Progressive evolution of a fault-related fold pair from growth strata geometries, Sant Llorenç de Morunys, SE Pyrenees. Journal of Structural Geology 19, 413-441.

Fossen, H., Schultz, R.A., Shipton, Z.K., Mair, K., 2007. Deformation bands in sandstone: a review. Journal of the Geological Society, London 164, 755-769.

Friedman, I., O'Neil, J.R., 1977. Compilation of stable isotope fractionation factors of geochemical interest, in: Fleischer, M. (Ed.), Data of Geochemistry, U. S. Gov. Print. Off. Washington D. C., pp. 1-12.

Friedman, M., Logan, J.M., 1977. Microscopic feather fractures Bull. Soc. Am. 81, 3417-3420.

García-Castellanos, D., Vergés, J., Gaspar-Escribano, J., Cloetingh, S., 2003. Interplay between tectonics, climate, and fluvial transport during the Cenozoic evolution of the Ebro Basin (NE Iberia). Journal of Geophysical Research 108, (B7), 2347

Geet, M.V., Swennen, R., Durmishi, C., Roure, F., Muchez, P., 2002. Paragenesis of Cretaceous to Eocene carbonate reservoirs in the Ionian fold and thrust belt (Albania): relation between tectonism and fluid flow. Sedimentology 49, 697-718.

Ghosh, P., Adkins, J., Affek, H., Balta, B., Guo, W., Schauble, E.A., Schrag, D., Eiler, J.M., 2006. 13C–18O bonds in carbonate minerals: A new kind of paleothermometer. Geochimia et Cosmochimica Acta 70, 1439-1456.

Goldstein, R.H., Reynolds, T.J., 1994. Sysematics of fluid inclusions in diagenetic minerals. SEPM Short Course Notes.

Grant, N.T., Banks, D.A., McCaig, A.M., Yardley, B.W.D., 1990. Chemistry, Source, and Behavior of Fluids Involved in Alpine Thrusting of the Central Pyrenees. Journal of Geophysical Research 95, 9123-9131.

Guo, W., Mosenfelder, J.L., Goddard, W.A., Eiler, J.M., 2009. Isotopic fractionations associated with phosphoric acid digestion of carbonate minerals: Insights from first-principles theoretical modeling and clumped isotope measurements. Geochimia et Cosmochimica Acta 73, 7203-7225.

Hanshaw, B.B., Coplen, T.B., 1973. Ultrafiltration by a compacted clay membrane II - Sodium ion exclusion at various ionic strengths Geochimia et Cosmochimica Acta 37, 2311-2327.

Henderson, I.H.C., McCaig, A.M., 1996. Fluid pressure and salinity variations in shear zone-related veins, central Pyrenees, France: Implications for the fault-valve model Tectonophysics 262, 321-348.

Heydari, E., 1997. Hydrotectonic models of burial diagenesis in platform carbonates based on formation water geochemistry in North American sedimentary basins, in: Montañez, I.P., Gregg, J.M., Shelton, K.L. (Eds.), Basin-wide diagenetic patterns: integrated petrologic, geochemical, and hydrologic considerations. Society of Economic Paleontologists and Mineralogists, Special Publication 57, p. 53 – 79.

Huntington, K.W., Eiler, J.M., Affeck, H.P., Guo, W., Bonifacie, M., Yeung, L.Y., Thiagarajan, N., Passey, B., Tripati, A., Daëron, M., Came, R., 2009. Methods and limitations of 'clumped' CO_2 isotope (Δ47) analysis by gas-source isotope ratio mass spectrometry. Journal of Mass Spectrometry 44, 1318-1329.

Katz, A., 1973. The interaction of magnesium with calcite during crystal growth at 25-90^{o}C and one atmosphere. Geochimia et Cosmochimica Acta 39, 486-508.

Kim, S.T., O'Neil, J.R., 1997. Equilibrium and nonequilibrium oxygen isotope effects in synthetic carbonates. Geochimia et Cosmochimica Acta 61, 3461.

Kinsman, D.J.J., 1969. Interpretation of Sr^{2+} concentrations in carbonate minerals and rocks. Journal of sedimentary Petrology 39, 486-508.

Kluge, T., John, C.M., Jourdan, A.L., Davis, S., Crawshaw, J., 2015. Laboratory calibration of the calcium carbonate clumped isotope thermometer in the 25-250 ^{o}C temperature range. Geochimia et Cosmochimica Acta 157, 213-227.

Knipe, R.J., McCaig, A.M., 1994. Microstructural and microchemical consequences of fluid flow in deforming rocks, in: Parnell, J. (Ed.), Geofluids: Origin, Migration and Evolution of Fluids in Sedimentary Basins. Geological Society, London, Special Publications, pp. 99-112.

Labaume, P., Berty, C., Laurent, P., 1991. Syn-digenetic evolution of shear structures in superficial nappes: an example from the Northern Apennines (NW Italy). Journal of Structural Geology 13, 385-398.

Lacombe, O., Swennen, R., Caracausi, A., 2014. Fluid–rock–tectonics interactions in basins and orogens. Marine and Petroleum Geology 55, 332 p.

Lacroix, B., Buatier, M., Labaume, P., Travé, A., Dubois, M., Charpentier, D., Ventalon, S., Convert-Gaubier, D., 2011. Microtectonic and geochemical characterization of thrusting in a foreland basin: Example of the South-Pyrenean orogenic wedge (Spain). Journal of Structural Geology 33, 1359-1377.

Laubach, S.E., Olson, J.E., Gross, M.R., 2009. Mechanical and fracture stratigraphy. AAPG Bulletin 93, 1413-1426.

Lefticariu, L., Perry, E.C., Fischer, M.P., Banner, J.L., 2005. Evolution of fluid compartmentalization in a detachment fold complex. Geology 33, 69-72.

Lewis, C.J., Vergés, J., Marzo, M., Heller, P.L., 1996. Youthful topography indicating active surface uplift in NE Iberia: Mantle upwelling along a leakly transform fault? Annales Geophysicae Suplement I, 14, C-204.

Losh, S., 1989. Fluid-rock interaction in an evolving ductile shear zone and across the brittle-ductile transition, central Pyrenees, France. American Journal of Science 289, 601-648.

Lyubetskaya, T., Ague, J.J., 2009. Modeling the Magnitudes and Directions of Regional Metamorphic Fluid Flow in Collisional Orogens. Journal of Petrology 50, 1505-1531.

Machel, H.G., Cavell, P.A., 1999. Low-flux, tectonically-induced sequeegee fluid flow ("hot flash") into the Rocky Mountain Foreland Basin. Bulletin of Canadian Petroleum Geology 47, 510-533.

Marshall, J.D., 1992. Climatic and oceanographic isotopic signals from the carbonate rock record and their preservation. Geological Magazine 129, 143-160.

McCaig, A.M., 1988. Deep fluid circulation in fault zones. Geology 16, 867-870.

McCaig, A.M., Wayne, D.M., Marshall, J.D., Banks, D., Henderson, I., 1995. Isotopic and fluid inclusion studies of fluid movement along the Gavarnie Thrust, central Pyrenees: Reaction fronts in carbonate mylonites. American Journal of Science 295, 309-343.

McCaig, A.M., Tritlla, J., Banks, D.A., 2000a. Fluid flow patterns during Pyrenean thrusting. Journal of Geochemical Exploration 69-70, 539-543.

McCaig, A.M., Tritlla, J., Banks, D.A., 2000b. Fluid mixing and recycling during Pyrenean thrusting: evidence from fluid inclusion halogen ratios. Geochimia et Cosmochimica Acta 64, 3395-3412.

McCrea, J.M., 1950. On the Isotopic Chemistry of Carbonates and a Paleotemperature Scale. Journal of Chemical Physics 18, 849-957.

McIntire, W.L., 1963. Trace element partition coefficients, a review of theory and applications to geology. Geochimia et Cosmochimica Acta 27, 1209-1264.

Meckler, A.N., Ziegler, M., Millán, M.I., Breitenbach, S.F., Bernasconi, S.M., 2014. Long-term performance of the Kiel carbonate device with a new correction scheme for clumped isotope measurements. Rapid Communications in Mass Spectrometry 28, 1705-1715.

Meyers, W.J., Lohmann, K.C., 1985. Isotope geochemistry of regionally extensive calcite cement zones and marine components in Mississipian limestones, New Mexico, in: Harris, O.M., Schneidermann, N. (Eds.), Carbonate Cements SEPM, Special Publications, pp. 223-239.

Morley, C.K., Warren, J., Tingay, M., Boonyasaknanon, P., Julapour, A., 2014. Comparison of modern fluid distribution, pressure and flow in sediments associated with anticlines growing in deepwater (Brunei) and continental environments (Iran). Marine and Petroleum Geology 51, 210-229.

Mucci, A., Morse, J.W., 1983. The incorporation of Mg2+ and Sr2+ into calcite overgrowths: Influences of growth rate and solution composition. Geochimia et Cosmochimica Acta 47, 217-233.

Muñoz, J.A., 1992. Evolution of a continental collision belt: ECORS–Pyrenees crustal balanced section, in: McClay, K.R. (Ed.), Thrust Tectonics. Chapman & Hall, London, pp. 235-246.

Muñoz, J.A., 2002. The Pyrenees, in: Gibbons, W., Moreno, T. (Eds.), The Geology of Spain. Geological Society, London, pp. 370-385.

Oberhänsli, H., Allen, P.A., 1987. Stable isotopic signatures of tertiary lake carbonates, eastern Ebro Basin, Spain. Palaeogeography, Palaeoclimatology, Palaeoecology 60, 59-75.

Ogata, K., Senger, K., Braathen, A., Tveranger, J., 2014. Fracture corridors as seal-bypass systems in siliciclastic reservoir-cap rock successions: Field-based insights from the Jurassic Entrada Formation (SE Utah, USA). Journal of Structural Geology 66, 162-187.

Oliver, J., 1986. Fluids expelled tectonically from orogenic belts: their role in hydrocarbon migration and other geologic phenomena. Geology 14, 99-102.

Passchier, C.W., Trouw, R.A.J., 2005. Microtectonics, 2 ed. Springer Berlin Heidelberg.

Puigdefàbregas, C., Muñoz, J.A., Marzo, M., 1986. Thrust Belt Development in the Eastern Pyrenees and Related Depositional Sequences in the Southern Foreland Basin, in: Allen, P.A., Homewood, P. (Eds.), Foreland Basins. Blackwell Publishing Ltd., Oxford, UK. , pp. 229-246.

Puigdefàbregas, C., Muñoz, J.A., Vergés, J., 1992. Thrusting and Foreland Basin Evolution in the Southern Pyrenees, in: McClay, K.R. (Ed.), Thrust Tectonics. London, Chapman & Hall, pp. 247-254.

Qing, H., Mountjoy, E., 1992. Large-scale fluid flow in the Middle Devonian Presqu'ile barrier, Western Canada Sedimentary Basin. Geology 20, 903-906.

Ramsay, J.G., 1980. The crack-seal mechanism of rock deformation. Nature 284, 135-139.

Reif, D., Decker, K., Grasemann, B., Peresson, H., 2012. Fracture patterns in the Zagros fold-and-thrust belt, Kurdistan Region of Iraq. Tectonophysics 576-577, 46-62.

Riba, O., 1973. Las discordancias sintectónicas del Alto Cardener (prepirineo catalán): ensayo de interpretación evolutiva. Acta Geologica Hispanica 8, 90-99.

Riba, O., 1976. Syntectonic unconformities of the Alto Cardener, Spanish Pyrenees: A genetic interpretation. Sedimentary Geology 15, 213-233.

Rosenbaum, G., Lister, G.S., Duboz, C., 2002. Relative motions of Africa, Iberia and Europe during Alpine orogeny. Tectonophysics 359, 117-129.

Roure, F., Choukroune, P., Berastegui, J., Muñoz, J.A., Villien, A., Matheron, P., Bareyt, M., Seguret, M., Camara, P., Deramond, J., 1989. Ecors deep seismic data and balanced cross sections: Geometric constraints on the evolution of the Pyrenees. Tectonics 8, 41-50.

Roure, F., Swennen, R., Schneider, F., Faure, J.L., Ferket, H., Guilhaumou, N., Osadetz, K., Robion, P., Vandeginste, V., 2005. Incidence and Importance of Tectonics and Natural Fluid Migration on Reservoir Evolution in Foreland Fold-and-Thrust Belts. Oil & Gas Science and Technology 60, 67-106.

Sáez, A., Anadón, P., Herrero, M.J., Moscariello, A., 2007. Variable style of transition between Paleogene fluvial fan and lacustrine systems, southern Pyrenean foreland, NE Spain. Sedimentology 54, 367-390.

Sans, M., 2003. From thrust tectonics to diapirism. The role of evaporites in the kinematic evolution of the eastern South Pyrenean front. Geologica Acta 1, 239-259.

Sans, M., Vergés, J., 1995. Fold development Related to Contractional Salt Tectonics: Southeastern Pyrenean Thrust Front, Spain., in: Jackson, M.P.A., Roberts, D.G., Snelson, S. (Eds.), Salt tectonics: a global perspective. AAPG Memoir, pp. 369-378.

Sans, M., Muñoz, J.A., Vergés, J., 1996. Triangle zone and thrust wedge geometries related to evaporitic horizons (Southern Pyrenees). Canadian Petroleum Geology Bulletin 4, 375-384.

Sanz, P., Pollard, D.D., Allwardt, P.F., Borja, R.I., 2008. Mechanical models of fracture reactivation and slip on bedding surfaces during folding of the asymmetric anticline at Sheep Mountain, Wyoming. Journal of Structural Geology 30, 1177-1191.

Segnit, E.R., Holland, H.D., Biscardi, C.J., 1962. The solubility of calcite in aqueous solutions-I The solubility of calcite in water between 75” and 200^{o} at CO2 pressures up to 60 atm Geochimia et Cosmochimica Acta 26, 1301-1331.

Séguret, M., 1972. Étude tectonique des nappes et séries décollées de la partie centrale du vesant sud des Pyrénées. Pub. USTELA, sér, Geol. Struct. n.2, Montpellier.

Serra-Kiel, J., Mató, E., Saula, E., Travé, A., Ferràndez-Cañadell, C., Àlvarez-Pérez, G., Franquès, J., Romero, J., 2003a. An inventory of the marine and transitional Middle/Upper Eocene deposits of the Southeastern Pyrenean Foreland Basin (NE Spain). Geologica Acta 1, 201-229.

Serra-Kiel, J., Travé, A., Mató, E., Saula, E., Ferràndez-Cañadell, C., Busquets, P., Tosquella, J., Vergés, J., 2003b. Marine and Transitional Middle/Upper Eocene Units of the Southeastern Pyrenean Foreland Basin (NE Spain). Geologica Acta 1, 177-200.

Shackleton, J.R., Cooke, M.L., Sussman, A.J., 2005. Evidence for temporally changing mechanical stratigraphy and effects on joint-network architecture. Geology 33, 101-104.

Sibson, R.H., 1981. Fluid Flow Accompanying Faulting: Field Evidence and Models, in: Simpson, D.W., Richards, P.G. (Eds.), Earthquake prediction. American Geophysical Union, pp. 593-603.

Sibson, R.H., 2005. Hinge-parallel fluid flow in fold-thrust belts: how widespread? Proceedings of the Geologists' Association 116, 301-309.

Srivastava, D.C., Engelder, T., 1990. Crack-propagation sequence and pore-fluid conditions during fault-bend folding in the Appalachian Valley and Ridge, central Pennsylvania. Geol. Soc. America Bull. 102, 116-128.

Stephenson, B.J., Koopman, A., Hillgartner, H., McQuillan, H., Bourne, S., Noad, J., Rawnsley, K., 2007. Structural and stratigraphic controls on fold-related fracturing in the Zagros Mountains, Iran: implications for reservoir development, in: Lonergan, L., Jolly, R.J.H., Rawnsley, K., Sanderson, D.J. (Eds.), Fractured reservoirs. Geological Society, London, Special Publications, pp. 1-21.

Suppe, J., Sábat, F., Muñoz, J.A., Poblet, J., Roca, E., Vergés, J., 1997. Bed-by-bed fold growth by kink-band migration: Sant Llorenç de Morunys, eastern Pyrenees. Journal of Structural Geology 19, 443-461.

Swanson, E.M., Wernicke, B.P., Eiler, J.M., Losh, S., 2012. Temperatures and fluids on faults based on carbonate clumped-isotope thermometry. American Journal of Science 312, 1-21.

Tavani, S., Storti, F., Lacombe, O., Corradetti, A., Muñoz, J.A., Mazzoli, S., 2015. A review of deformation pattern templates in foreland basin systems and fold-and-thrust-belts: Implications for the state of stress in the frontal regions of thrust wedges. Earth-Science Reviews 141, 82-104.

Taylor, B.E., 1987. Stable isotope geochemistry of ore-forming fluids, in: Kyser, T.K. (Ed.), Short Course in Stable Isotope Geochemistry of low Temperature Fluids. Mineral Association of Canada, pp. 337-418.

Tempest, S.A., 1991. Fluid-rock interaction in ductile shear zones, central-eastern Pyrenees. PhD thesis, Leeds University, 202 p.

Travé, A., Calvet, F., 2001. Syn-rift geofluids in fractures related to the early-middle Miocene evolution of the Vallès-Penedès half-graben (NE Spain). Tectonophysics 336, 101-120.

Travé, A., Labaume, P., Calvet, F., Soler, A., 1997. Sediment dewatering and pore fluid migration along thrust faults in a foreland basin inferred from isotopic and elemental geochemical analyses (Eocene southern Pyrenees, Spain). Tectonophysics 282, 375-398.

Travé, A., Labaume, P., Calvet, F., Soler, A., Tritlla, J., Bautier, M., Potdevin, J.L., Séguret, M., Raynaud, S., Briqueu, L., 1998a. Fluid migration during Eocene thrust emplacement in the south Pyrenean foreland basin (Spain): an integrated structural, mineralogical and geochemical approach, in: Mascle, A., Puigdefàbregas, C., LuterBacher, H.P., Fernàndez, M. (Eds.), Cenozoic Foreland Basins of Western Europe. Geological Society, Special Publications, pp. 163-188.

Travé, A., Calvet, F., Soler, A., Labaume, P., 1998b. Fracturing and fluid migration during Paleogene compression and Neogene extension in the Catalan Coastal Ranges, Spain. Sedimentology 45, 1063-1082.

Travé, A., Calvet, F., Sans, M., Vergés, J., Thirlwall, M., 2000. Fluid history related to the Alpine compression at the margin of the south-Pyrenean Foreland basin: the El Guix anticline. Tectonophysics 321, 73-102.

Travé, A., Calvet, F., Salas, R., Playà, E., 2004. Fluid Flow during Paleogene Compression in the Linking Zone Fold and Thrust Belt (Northeast Spain), in: Swennen, R., Roure, F., Granath, J.W. (Eds.), Deformation, fluid flow, and reservoir appraisal in foreland fold and thrust belts. AAPG Hedberg Series, pp. 215-243.

Travé, A., Labaume, P., Vergés, J., 2007. Fluid systems in Foreland Fold and thrust belts: an overview from the Southern Pyrenees, in: Lacombe, O., Lavé, J., Roure, F., Vergés, J. (Eds.), Thrust Belts and Foreland Basins: From Fold Kinematics to Hydrocarbon Systems. Springer, pp. 93-115.

Treagus, S.H., 1988. Strain refraction in layered systems. Journal of Structural Geology 19, 551-566.

Tucker, M.E., Wright, P.V., 1990. Carbonate Sedimentology. Blackwell, Oxford.

Vajdova, V., Zhu, W., Chen, T.Z.N., Wong, T.F., 2010. Micromechanics of brittle faulting and cataclastic flow in Tavel limestone. Journal of Structural Geology 32, 1158-1169.

Valero, L., Garcés, M., Cabrera, L., Costa, E., Sáez, A., 2014. 20 Myr of eccentricity paced lacustrine cycles in the Cenozoic Ebro Basin Earth and Planetary Science Letters 408, 183-193.

Vandeginste, V., Swennen, R., Allaeys, M., Ellam, R.M., Osadetz, K., Roure, F., 2012. Challenges of structural diagenesis in foreland fold-and-thrust belts: A case study on paleofluid flow in the Canadian Rocky Mountains West of Calgary. Marine and Petroleum Geology 35, 235-251.

Vergés, J., 1993. Estudi geològic del vessant sud del Pirineu oriental i central. Evolució cinemàtica en 3D. PhD thesis, Universitat de Barcelona, Barcelona, Spain, 203 p.

Vergés, J., Martínez, A., Muñoz, J.A., 1992. South Pyrenean fold and thrust belt: The role of foreland evaporitic levels in thrust geometry, in: McClay, K. (Ed.), Thrust Tectonics. London, Chapman & Hall, pp. 255-264.

Vergés, J., Marzo, M., Santaeulària, T., Serra-Kiel, J., Burbank, D.W., Muñoz, J.A., Giménez-Montsant, J., 1998. Quantified vertical motions and tectonic evolution of the SE Pyrenean foreland basin, in: Mascle, A., Puigdefàbregas, C., Luterbacher, H.P., Fernàndez, M. (Eds.), Cenozoic Foreland Basins of Western Europe. Geological Society Special Publications, pp. 107-134.

Vergés, J., Marzo, M., Muñoz, J.A., 2002a. Growth strata in foreland settings. Sedimentary Geology 146, 1-9.

Vergés, J., Fernàndez, M., Martínez, A., 2002b. The Pyrenean orogen: pre-, syn-, and post-collisional evolution, in: Rosenbaum, G., Lister, G. (Eds.), Reconstruction of the evolution of the Alpine-Himalayan Orogen. Journal of the Virtual Explorer, pp. 55-74.

Vilasi, N., Malandain, J., Barrier, L., Callot, J.P., Amrouch, K., Guilhaumou, N., Lacombe, O., Muska, K., Roure, F., Swennen, R., 2009. From outcrop and petrographic studies to basin-scale fluid flow modelling: The use of the Albanian natural laboratory for carbonate reservoir characterisation. Tectonophysics 474, 367-392.

Wacker, U., Fiebig, J., Schoene, B.R., 2013. Clumped isotope analysis of carbonates: comparison of two different acid digestion techniques. Rapid Communications in Mass Spectrometry 27, 1631-1642.

Watkins, H., Butler, R.W.H., Bond, C.E., Healy, D., 2015. Influence of structural position on fracture networks in the Torridon Group, Achnashellach fold and thrust belt, NW Scotland. Journal of Structural Geology 74, 64-80.

Wickham, S.M., Taylor, H.P., 1985. Stable isotopic evidence for large-scale seawater infiltration in a regional metamorphic terrane; the Trois Seigneurs Massif, Pyrenees, France. Contributions to Mineralogy and Petrology 91, 122-137.

Wickham, S.M., Taylor, H.P., 1987. Stable isotope constraints on the origin and depth of penetration of hydrothermal fluids associated with Hercynian regional metamorphism and crustal anatexis in the Pyrenees. Contributions to Mineralogy and Petrology 95, 255-268.

Williams, E.A., Ford, M., Vergés, J., Artoni, A., 1998. Alluvial gravel sedimentation in a contractional growth fold setting, Sant Llorenç de Morunys, southeastern Pyrenees, in: Mascle, A., Puigdefàbregas, C., Luterbacher, H.P., Fernàndez, M. (Eds.), Cenozoic Foreland Basins of Western Europe., Geological Society Special Publications, pp. 69-106.

Fig. 1

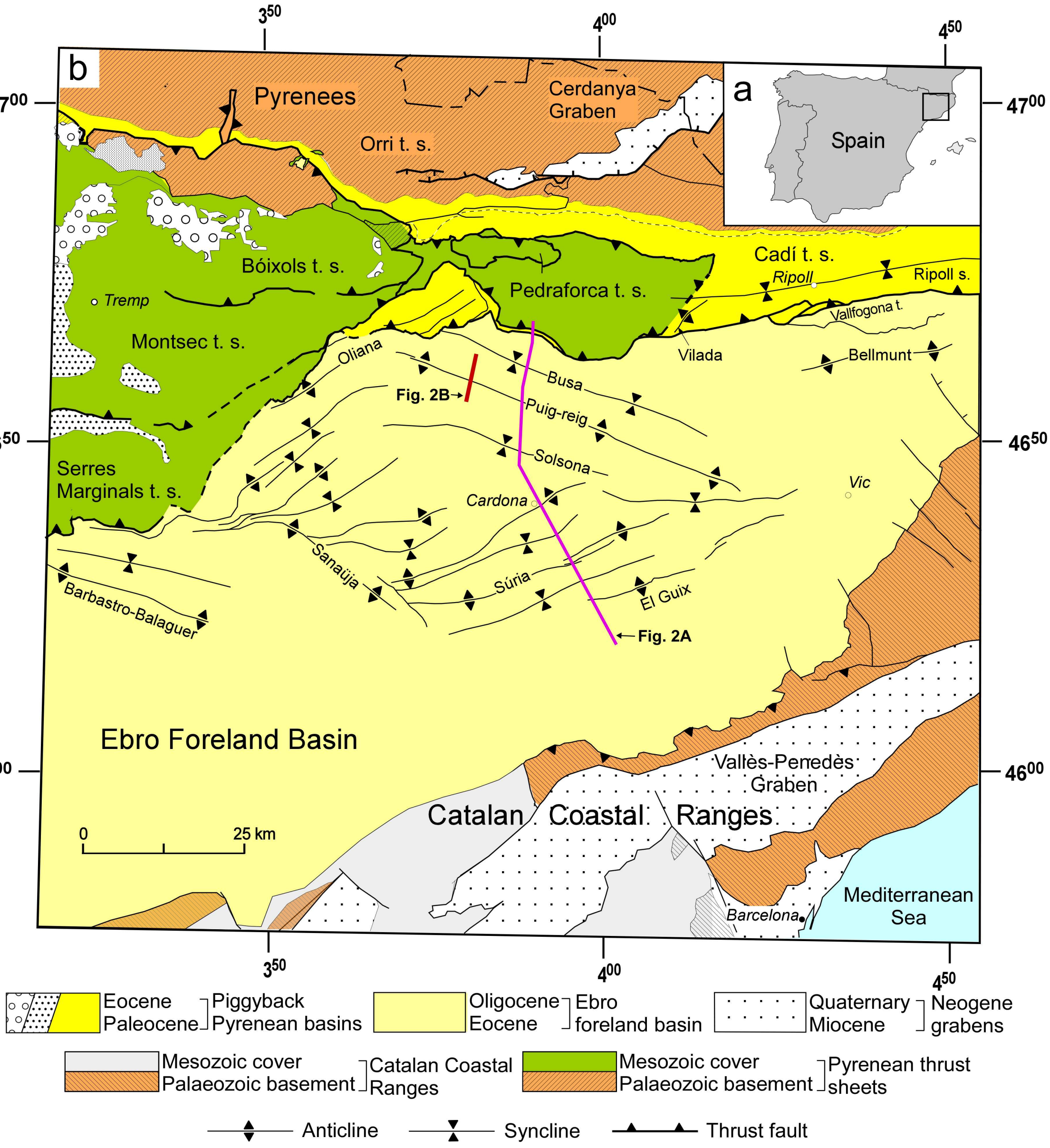
b
a
Spain
Pyrenees
Orri t. s.
Cerdanya Graben
Bóixols t. s.
Tremp
Montsec t. s.
Pedraforca t. s.
Cadí t. s.
Ripoll
Ripoll s.
Vallfogona t.
Vilada
Bellmunt
Oliana
Busa
Puig-reig
Solsona
Cardona
Fig. 2B
Fig. 2A
Vic
Serres Marginals t. s.
Sanaüja
Súria
El Guix
Barbastro-Balaguer
Ebro Foreland Basin
Vallès-Penedès Graben
Catalan Coastal Ranges
Barcelona
Mediterranean Sea
0
25 km
Eocene
Paleocene
Piggyback Pyrenean basins
Oligocene
Eocene
Ebro foreland basin
Quaternary
Miocene
Neogene grabens
Mesozoic cover
Palaeozoic basement
Catalan Coastal Ranges
Mesozoic cover
Palaeozoic basement
Pyrenean thrust sheets
Anticline
Syncline
Thrust fault

Fig. 2

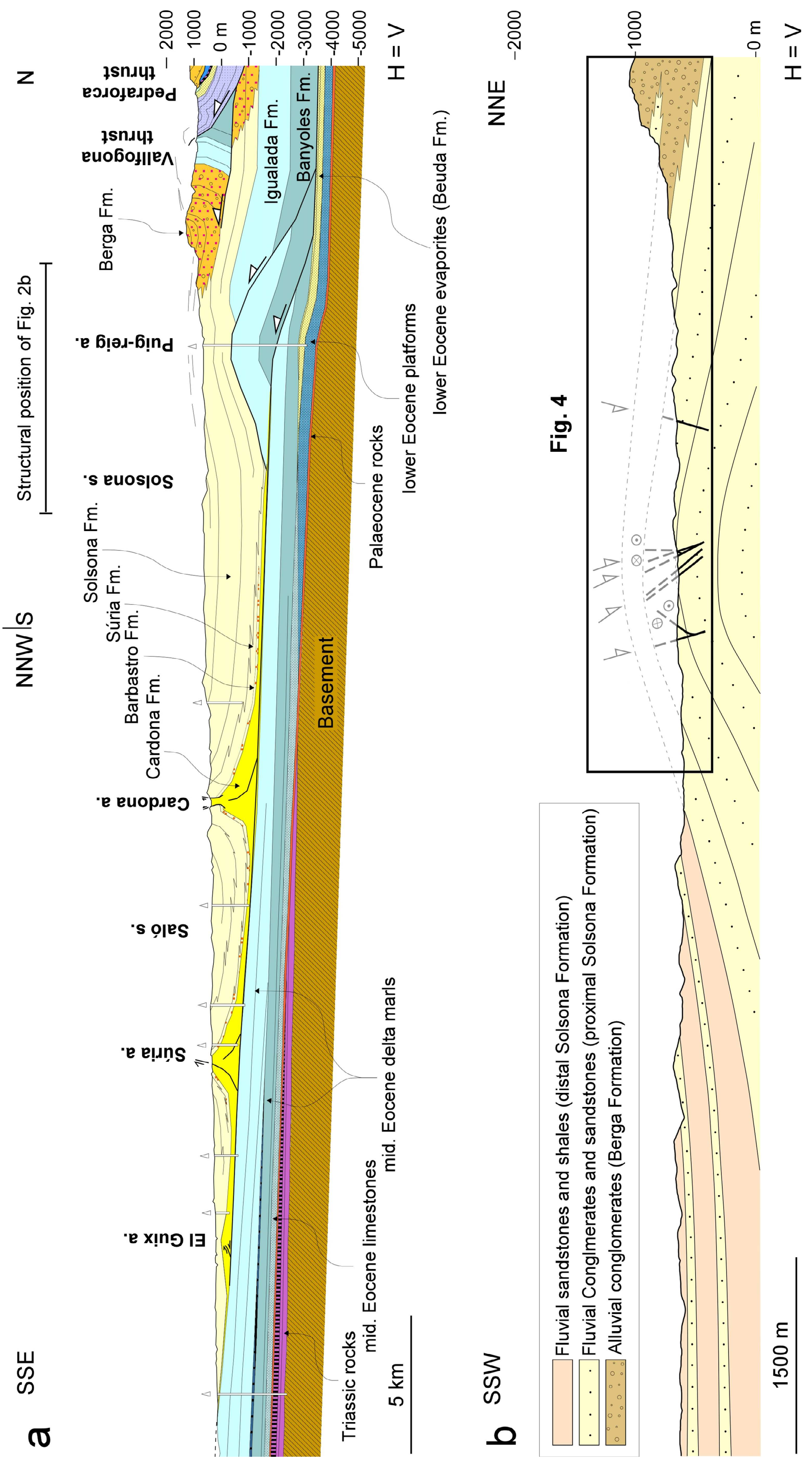

a
SSE
NNW|S
N
Structural position of Fig. 2b
El Guix a.
Súria a.
Saló s.
Cardona a.
Solsona s.
Puig-reig a.
Berga Fm.
Vallfogona thrust
Pedraforca thrust
Solsona Fm.
Súria Fm.
Barbastro Fm.
Cardona Fm.
Igualada Fm.
Banyoles Fm.
Basement
Triassic rocks
mid. Eocene limestones
mid. Eocene delta marls
Palaeocene rocks
lower Eocene platforms
lower Eocene evaporites (Beuda Fm.)
2000
1000
0 m
-1000
-2000
-3000
-4000
-5000
H = V
5 km
b
SSW
NNE
-2000
-1000
-0 m
Fig. 4
Fluvial sandstones and shales (distal Solsona Formation)
Fluvial Conglmerates and sandstones (proximal Solsona Formation)
Alluvial conglomerates (Berga Formation)
1500 m

Fig. 3

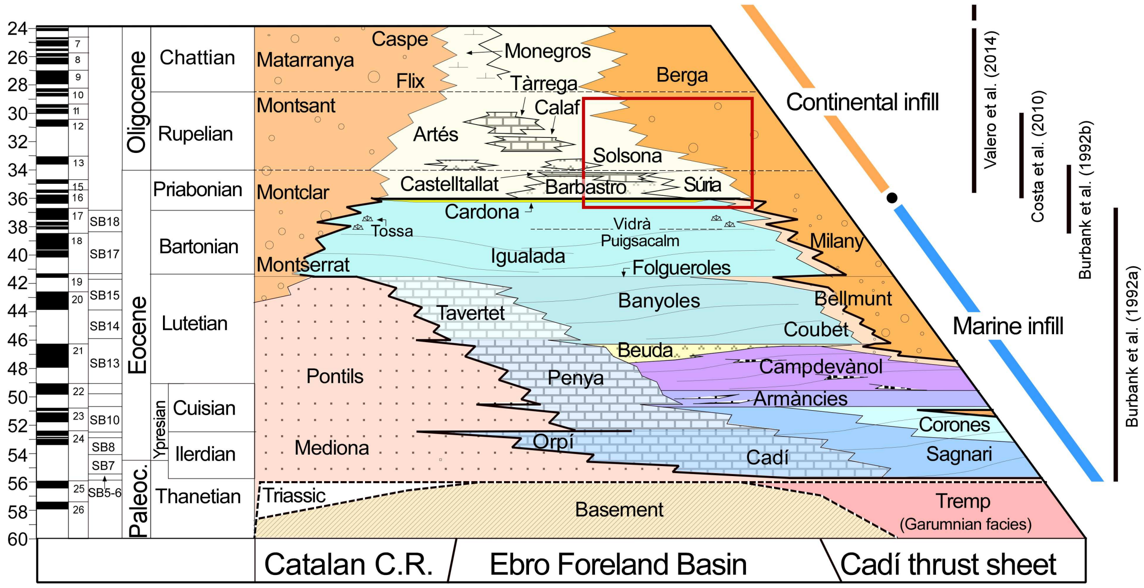

Oligocene
Eocene
Paleoc.
Ypresian
Chattian
Rupelian
Priabonian
Bartonian
Lutetian
Cuisian
Ilerdian
Thanetian
SB18
SB17
SB15
SB14
SB13
SB10
SB8
SB7
SB5-6
Matarranya
Caspe
Monegros
Flix
Tàrrega
Berga
Montsant
Calaf
Artés
Solsona
Castelltallat
Barbastro
Súria
Montclar
Cardona
Tossa
Vidrà
Puigsacalm
Milany
Igualada
Folgueroles
Montserrat
Bellmunt
Banyoles
Tavertet
Coubet
Beuda
Campdevànol
Pontils
Penya
Armàncies
Corones
Mediona
Orpí
Cadí
Sagnari
Triassic
Basement
Tremp
(Garumnian facies)
Catalan C.R.
Ebro Foreland Basin
Cadí thrust sheet
Continental infill
Marine infill
Valero et al. (2014)
Costa et al. (2010)
Burbank et al. (1992b)
Burbank et al. (1992a)

1090 Fig. 4

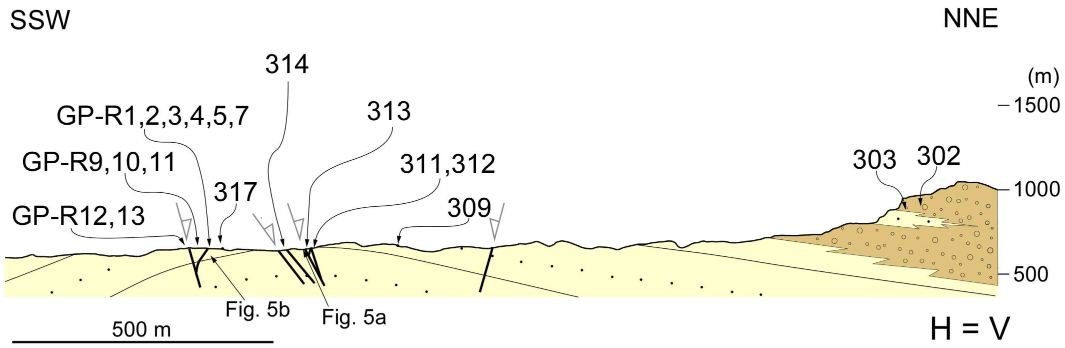

1091

Fig. 5

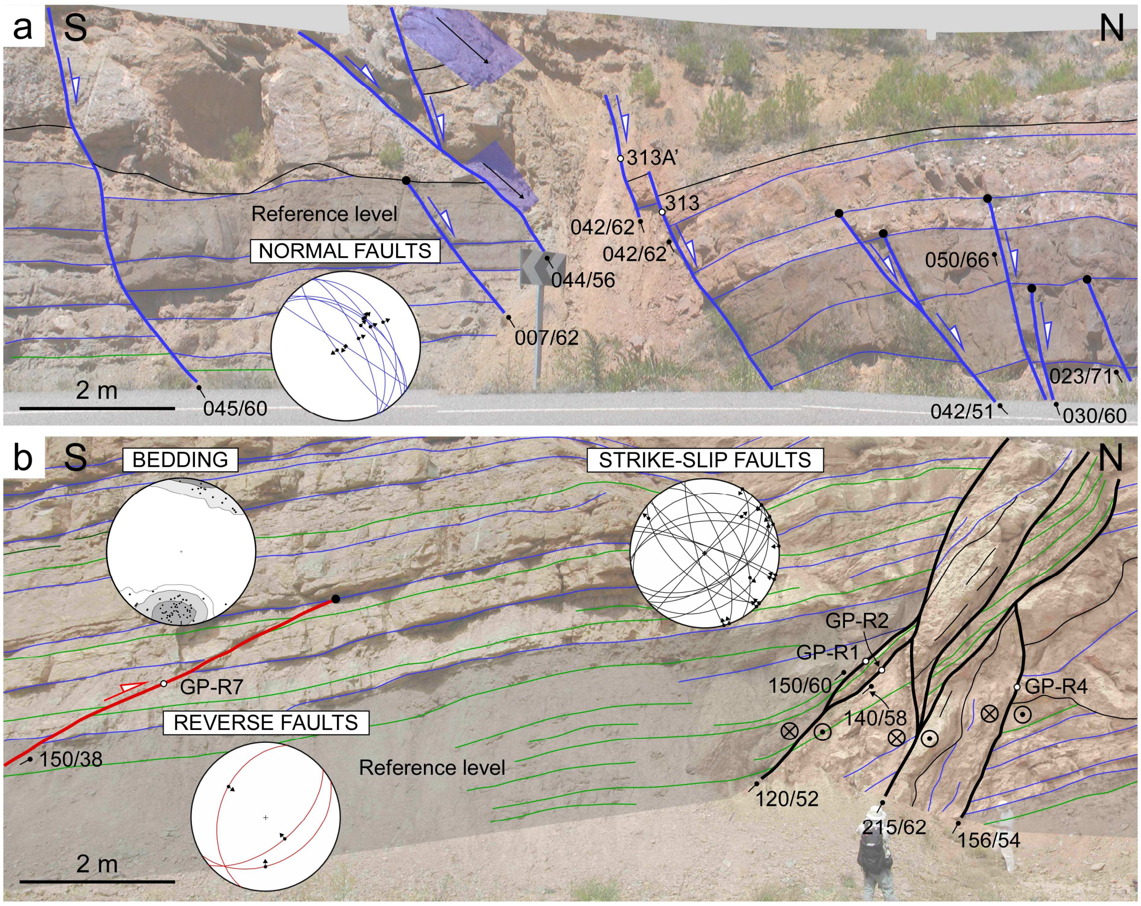

a
S
N
313A'
313
042/62
042/62
Reference level
NORMAL FAULTS
044/56
007/62
050/66
023/71
042/51
030/60
045/60
2 m
b
S
BEDDING
STRIKE-SLIP FAULTS
N
GP-R2
GP-R1
150/60
140/58
GP-R4
GP-R7
REVERSE FAULTS
150/38
Reference level
120/52
215/62
156/54
2 m

1094 Fig. 6

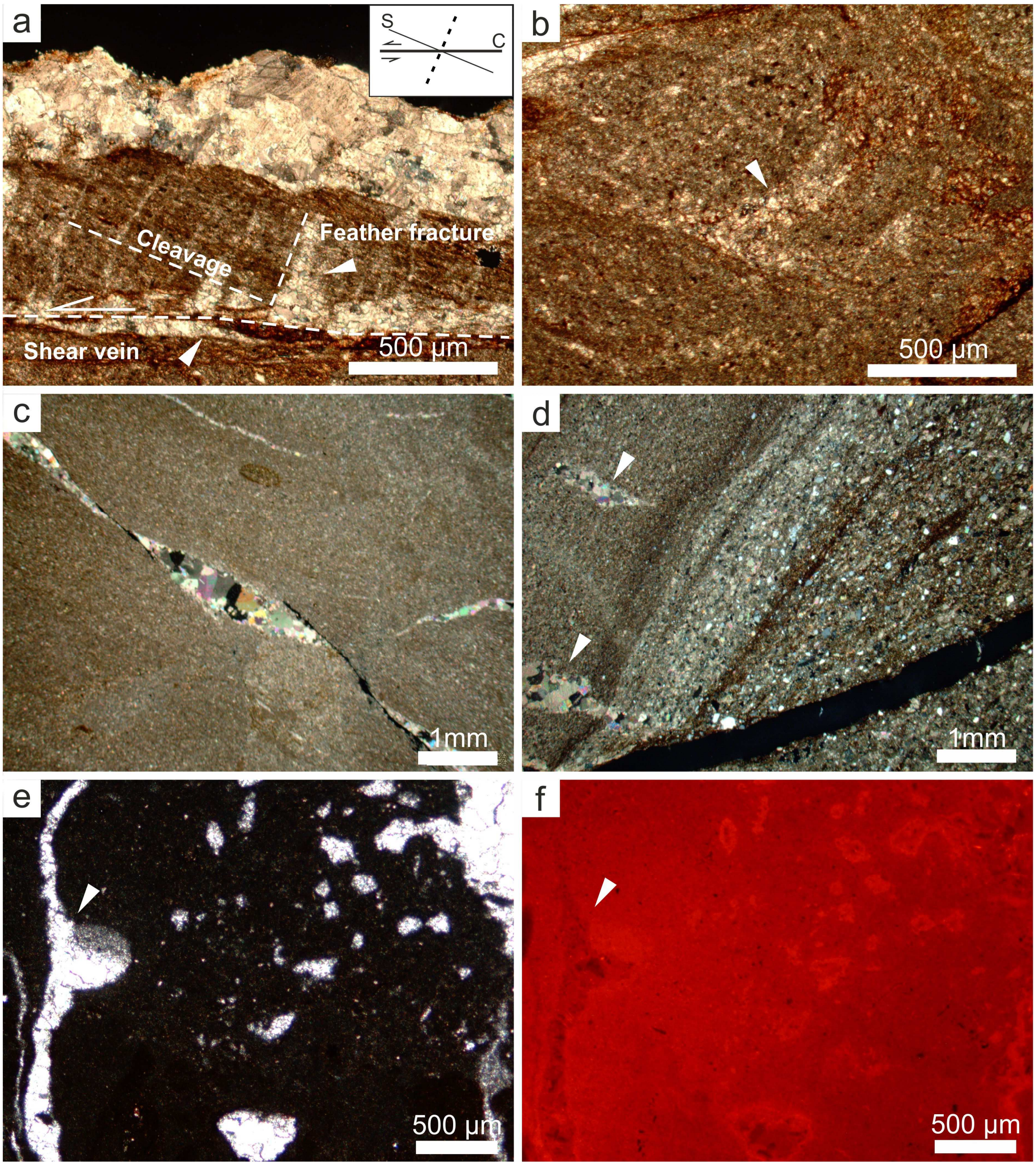

1095

Fig. 7

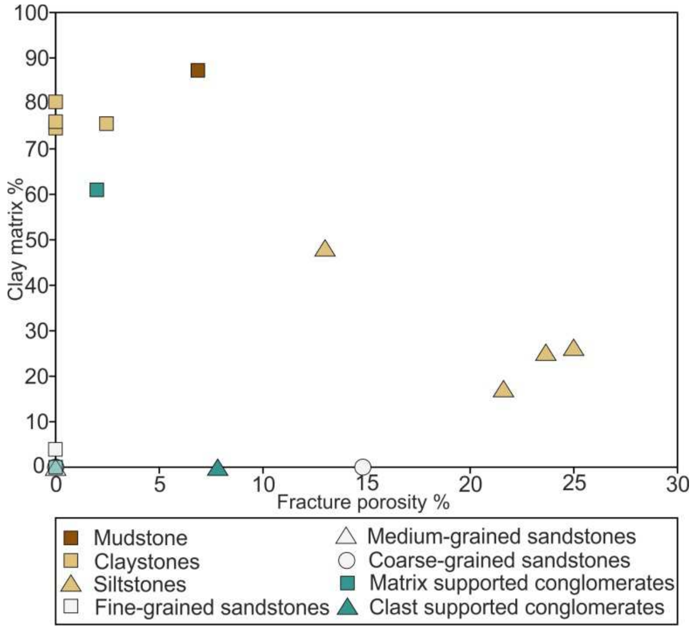
Clay matrix %
Fracture porosity %
0
10
20
30
40
50
60
70
80
90
100
0
5
10
15
20
25
30
Mudstone
Claystones
Siltstones
Fine-grained sandstones
Medium-grained sandstones
Coarse-grained sandstones
Matrix supported conglomerates
Clast supported conglomerates

Fig. 8

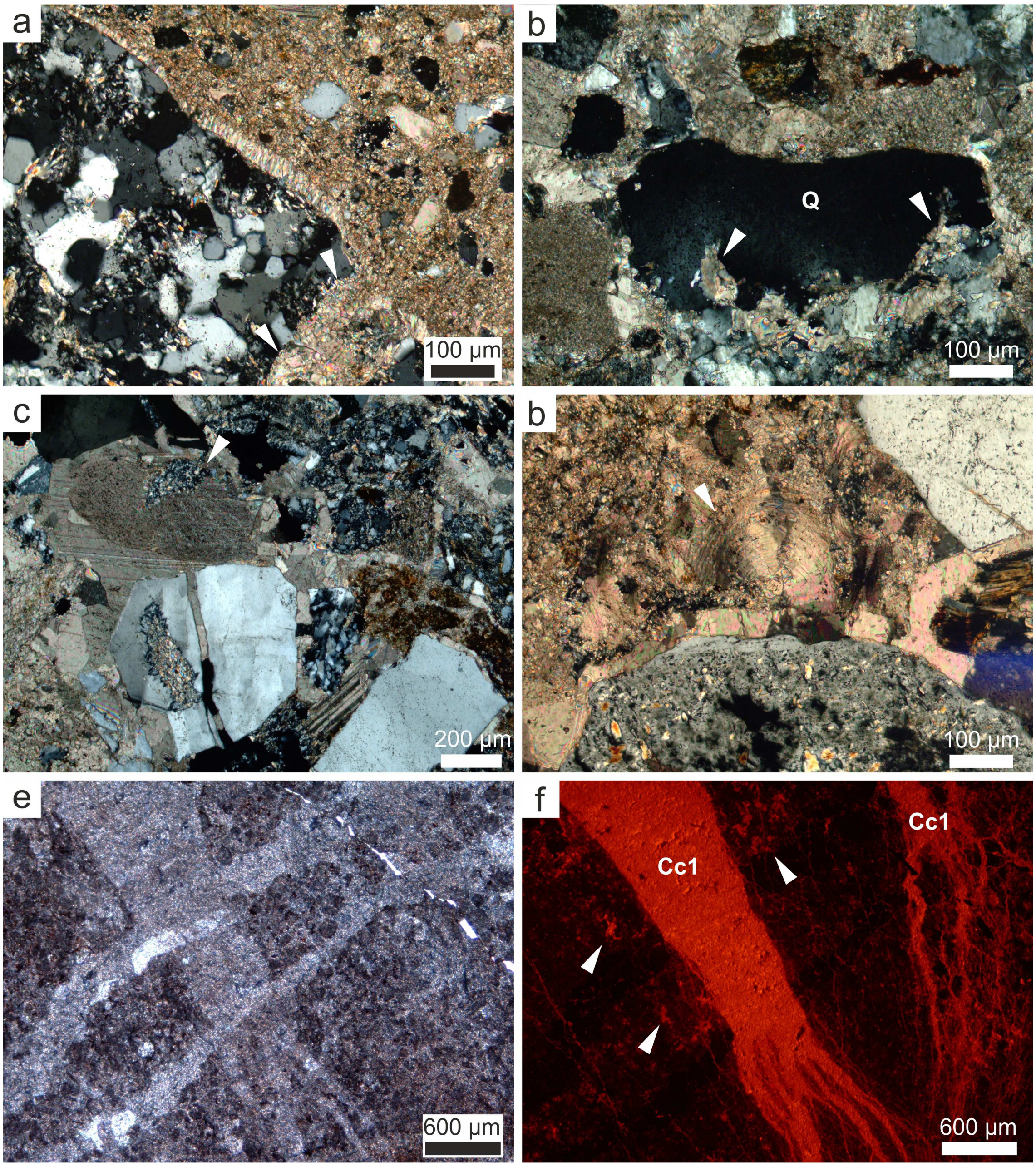

1100 Fig. 9

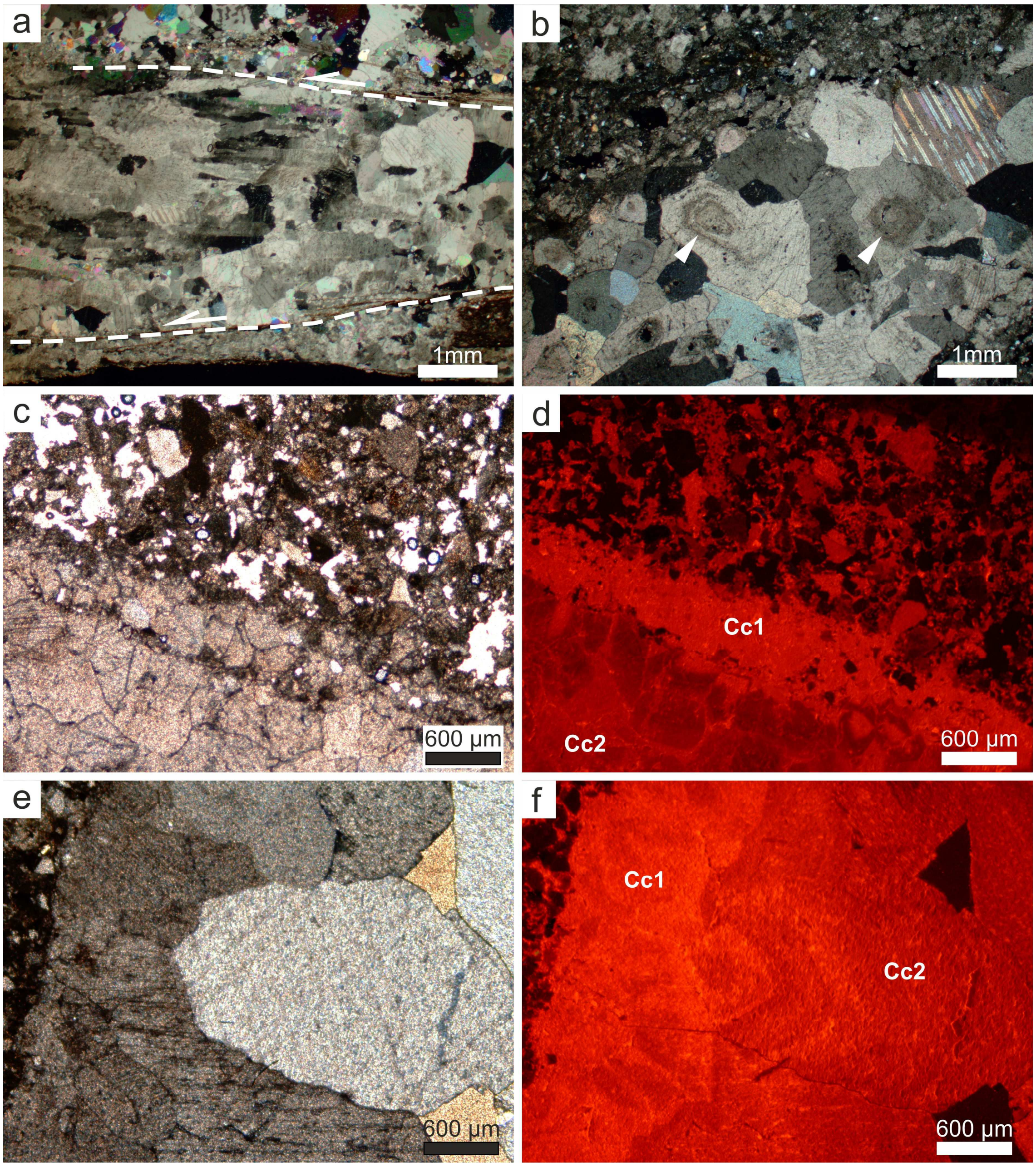

1101

Fig. 10

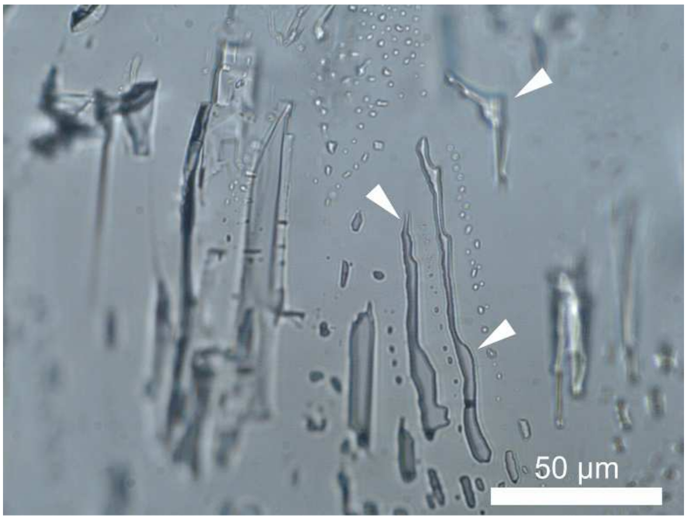

1104 Fig. 11

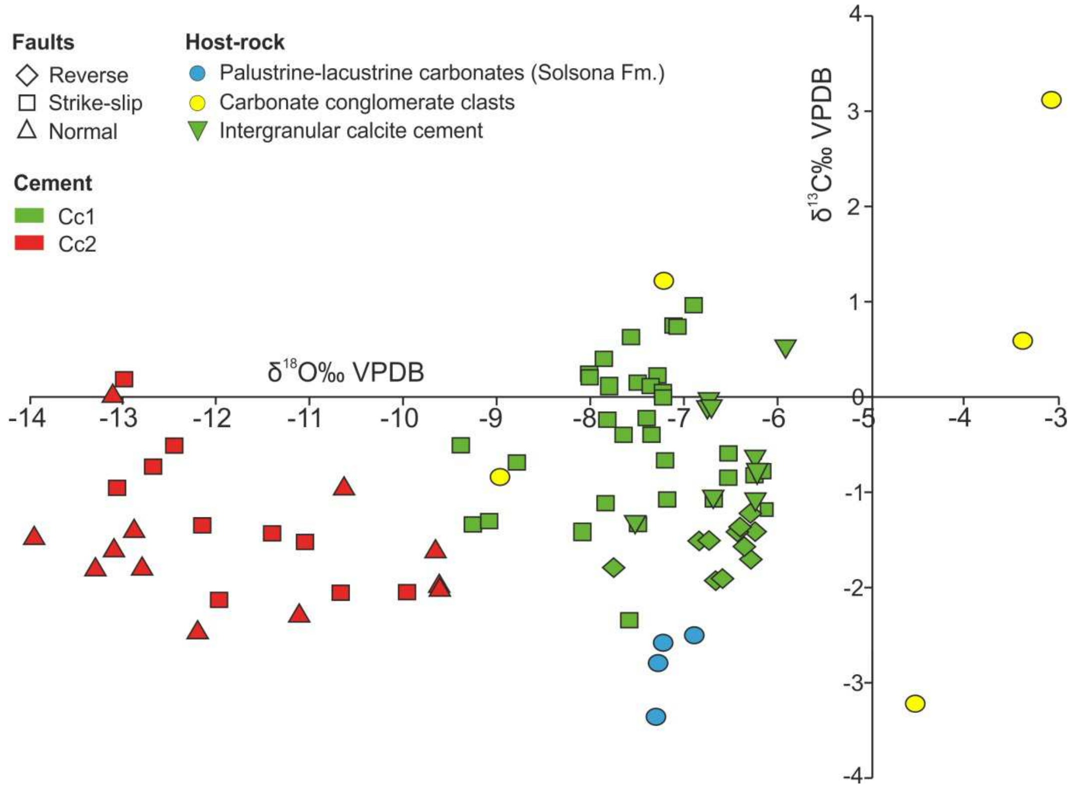

1105

Fig. 12

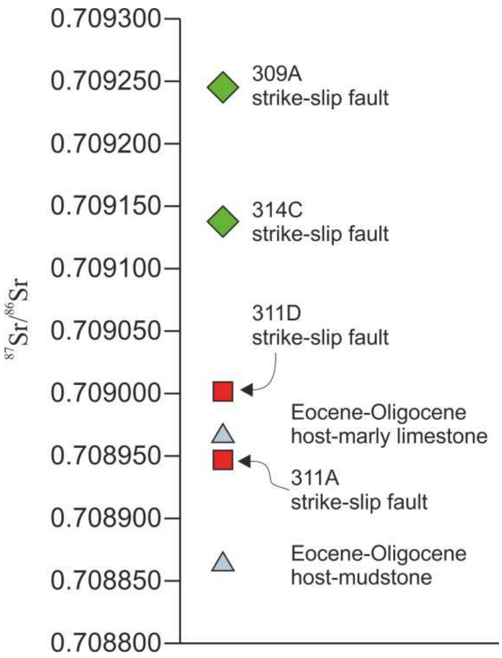
0.709300
0.709250
0.709200
0.709150
0.709100
0.709050
0.709000
0.708950
0.708900
0.708850
0.708800
$^{87}Sr/^{86}Sr$
309A
strike-slip fault
314C
strike-slip fault
311D
strike-slip fault
Eocene-Oligocene
host-marly limestone
311A
strike-slip fault
Eocene-Oligocene
host-mudstone

Fig. 13

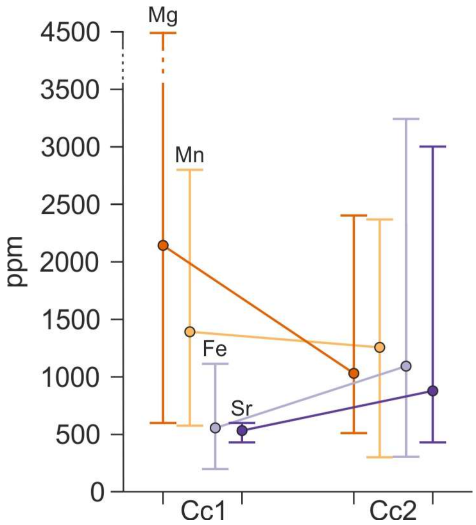

Fig. 14

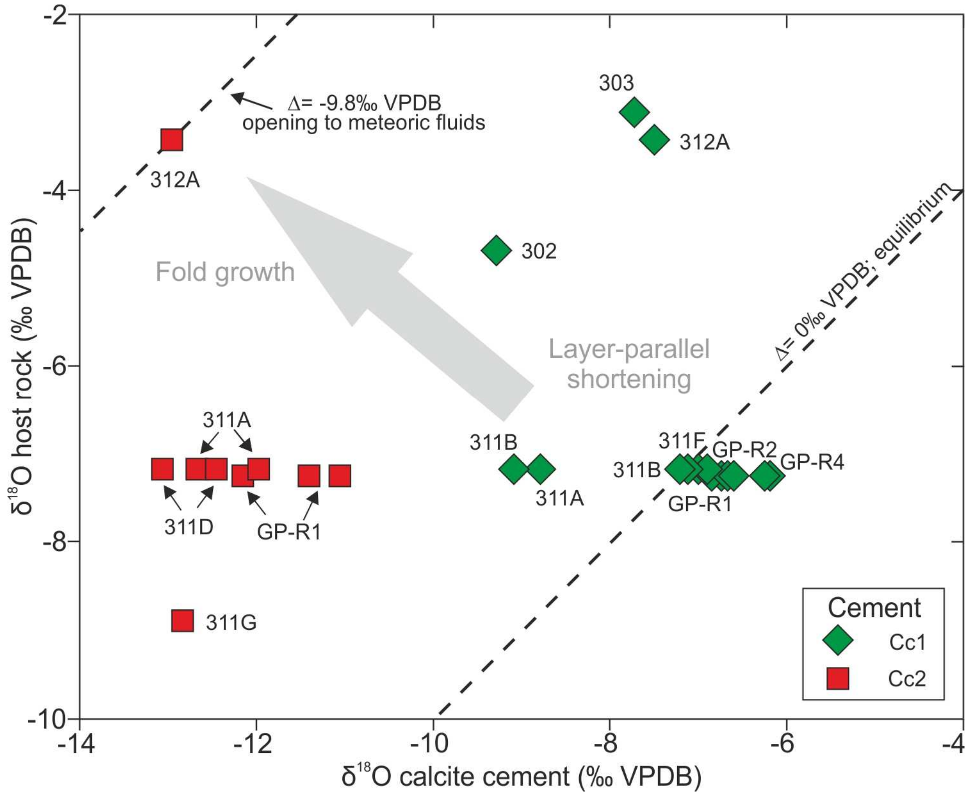

Δ= -9.8‰ VPDB
opening to meteoric fluids
Fold growth
Layer-parallel
shortening
Δ= 0‰ VPDB; equilibrium
303
312A
302
311B
311A
311F
GP-R2
GP-R4
GP-R1
311D
311G
Cement
Cc1
Cc2
-2
-4
-6
-8
-10
-14
-12
-10
-8
-6
-4
δ18O host rock (‰ VPDB)
δ18O calcite cement (‰ VPDB)

1112 Fig. 15

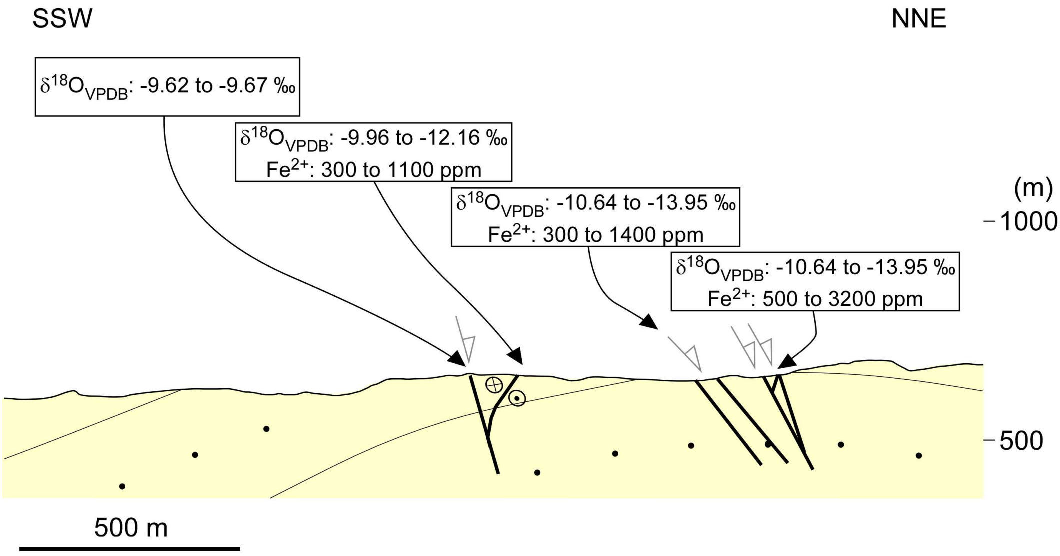

1113

Fig. 16

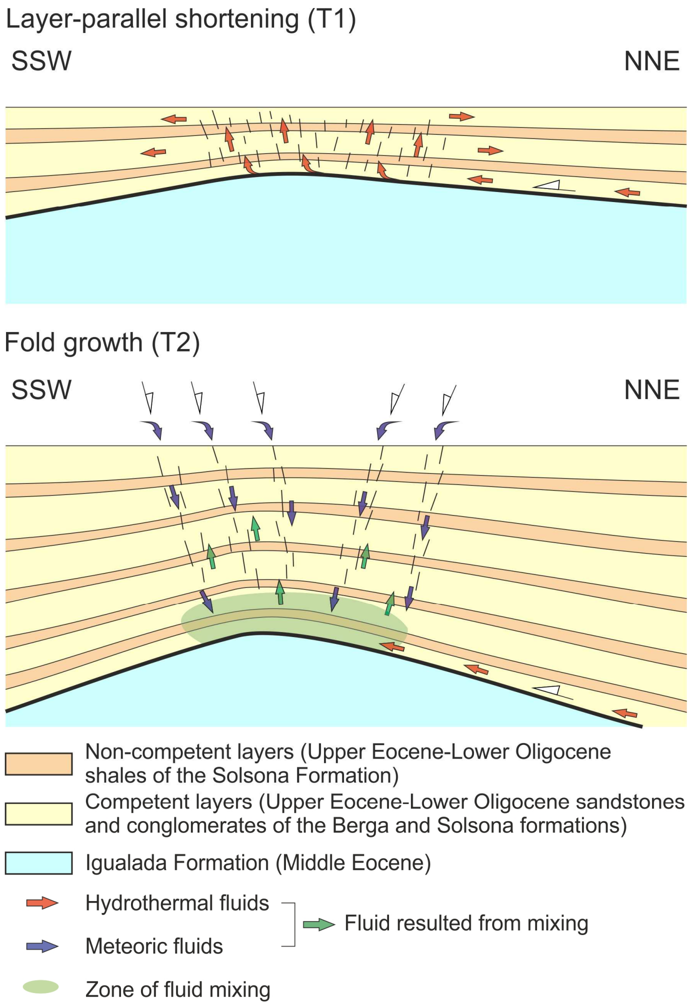

Layer-parallel shortening (T1)
SSW
NNE
Fold growth (T2)
SSW
NNE
Non-competent layers (Upper Eocene-Lower Oligocene shales of the Solsona Formation)
Competent layers (Upper Eocene-Lower Oligocene sandstones and conglomerates of the Berga and Solsona formations)
Igualada Formation (Middle Eocene)
Hydrothermal fluids
Meteoric fluids
Fluid resulted from mixing
Zone of fluid mixing

1116 Fig. 17

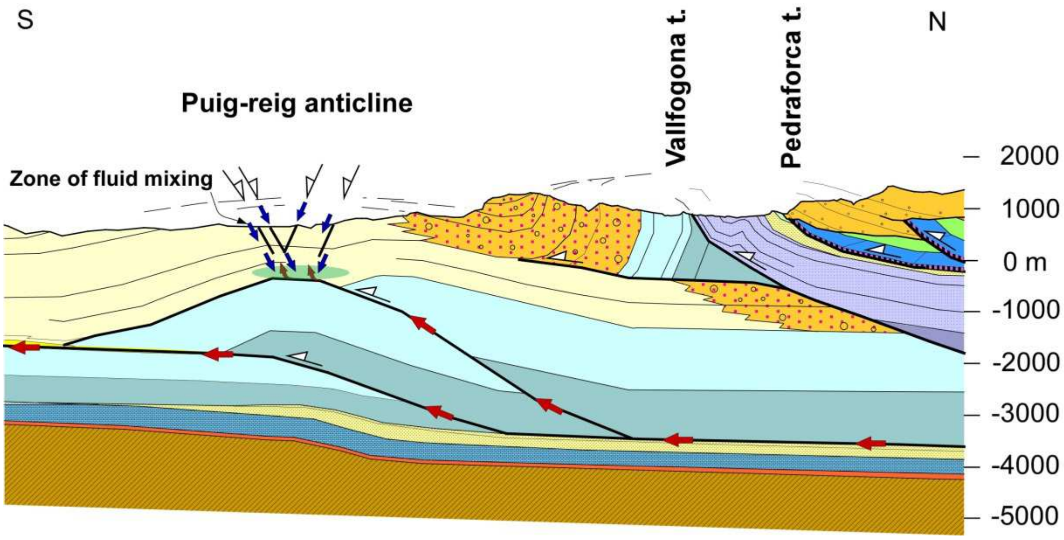

1117

Fig. 1 (a) Regional map of the Iberian Peninsula showing the location of the South Pyrenean fold and thrust belt (black box; Fig 1b). (b) Simplified geological map of the main structural units of the South Pyrenean fold and thrust belt (Vergés, 1993). The purple line shows the trace of the geological cross section shown in Fig. 2a. The thick red line shows the study area.

Fig. 2 (a) Geological cross section of the frontal part of the South Pyrenean fold and thrust belt (Vergés, 1993). The horizontal black line shows the structural position of Fig. 2b. (b) Geological cross section of the Puig-reig anticline performed in this work. Faults are drafted according to true dips. The black box indicates the location of Fig. 4.

Fig. 3 N-S stratigraphic panel of the eastern Pyrenees and the eastern Ebro Foreland Basin modified from Vergés et al. (1998). The age of sedimentary units has been defined according to Burbank et al. (1992a, b), Costa et al. (2010) and Valero et al. (2014). The sedimentary record of the foreland basin is separated in Paleocene to upper Eocene marine sediments and upper Eocene to upper Oligocene continental sediments. The red box indicates the sedimentary units in the frontal part of the South Pyrenean fold and thrust belt.

Fig. 4 Detail of Fig. 2b where are shown the sampled structures in this work.

Fig. 5 Outcrop interpretation of the main structural features observed in the Puig-reig anticline. (a) Normal faults (thick blue lines) affecting the forelimb close to the hinge of the Puig-reig anticline. (b) Strike-slip (thick black lines) and reverse (thick red line) faults affecting the forelimb of the Puig-reig anticline. Thin black, blue and green lines represent conglomerates, sandstones and lutite layers, respectively. Dip directions and dips of faults are given. White points show sample locations. Stereograms for all bedding and fault dips and fault striae sets measured in the studied section of the Puig-reig anticline are given. Bedding dips are plotted as lines.

Fig. 6 Images from polarizing optical microscope and cathodoluminescence (CL) of the main features of the microstructures affecting the studied host rocks. (a) Sample GP-R11. Calcite shear vein with an associated microscopic feather fracture (crossed nicols). Note how cleavage perpendicular to the extensional fracture walls is developed in the host rock. (b) Sample GP-R11. Irregular extension vein (white triangle) affecting a siltstone layer (crossed nicols). Note how the contact of cement with the host rock is fuzzy. (c) Sample GP-R7. Dilational jog filled by blocky calcite (crossed nicols). (d) Sample GP-R2. Bedding-perpendicular veins (white triangles) (crossed nicols). (e) Sample GP-R4. Vein interconnected with a void filled by calcite cement displaying geopetal structures (white triangle). (f) Sample GP-R4. CL image of Fig. 6e (white triangle). Note how the vein and the void are filled by the same calcite cement.

Fig. 7 Fracture porosity vs clay matrix content cross-plot. For each type of host rock the following samples have been analyzed by point counting: Mudstone (GP-R4); Claystones (GP-R2, 303 and 317); Siltstones (GP-R2, GP-R7, GP-R9 and GP-R10); Fine-grained sandstones (309A, 309B, 313A, 314D1 and 314D2); Medium-grained sandstones (311A, 311B, 312A and 314C; Coarse-grained sandstones (GP-R5 and GP-R12); Matrix supported conglomerates (GP-R13, 302 and 311F); Clast supported conglomerates (314A).

Fig. 8 Images from polarizing optical microscope and cathodoluminescence (CL) of the main replacement textures observed in host rocks. (a) Sample GP-R13. Calcite cement replacing partially a conglomerate clast made of polycrystalline quartz (white arrows). Note how the contact between silicic clast and conglomerate matrix is open and filled by calcite cement (crossed nicols). (b) Sample GP-R5. Protrusions of calcite (white triangles) into a quartz grain (Q) indicating replacement of detrital quartz (crossed nicols). (c) Sample GP-R12. Calcite cement Cc1 replacing a detrital grain (crossed nicols). Note how a remnant of de replaced grain is preserved (white triangle). (d) Sample GP-R12. Replacement of fibrous spherulite by calcite (crossed nicols). (e-f) Sample 302. CL image of a dolomite conglomerate clast (non-luminescent) affected by a vein filled by cement Cc1. Patches of microsparite with the same luminescence of Cc1 cement (white triangles) are developed in the conglomerate clast.

Fig. 9 Images from polarizing optical microscope and cathodoluminescence (CL) of the main features of calcite cements. (a) Sample GP-R1. Shear vein (white dashed line) filled by fibrous sparite passing laterally to blocky calcite (crossed nicols). (b) Sample 311A. Blocky calcite cement with growth zonation present in some crystals (white triangles). (c-d) Sample 311A. CL image where is shown the sharp contact between cements Cc1 and Cc2. (e-f) Sample 314D2. CL image where is shown the gradual change from calcite cement Cc1 to Cc2.

Fig. 10 Sample 311D. Image of optical microscope where is show a fluid inclusion assemblage. Note how fluid inclusions are stretched, showing an irregular shape (white triangles).

Fig. **11** $\delta^{18}O$ vs $\delta^{13}C$ cross-plot of carbonate host rocks and calcite cements of the Puig-reig anticline.

Fig. **12** $^{87}Sr/^{86}Sr$ composition of the calcite cements and carbonate host rocks. Green diamonds represent veins with calcite cement Cc1. Red squares represent veins with calcite cement Cc2. Blue triangles represent palustrine-lacustrine carbonates.

Fig. 13 Elemental composition of the calcite cements. For Mg, Mn, Fe and Sr. Minimum, maximum and mean contents are given.

Fig. 14 δ18O calcite cement vs δ18O host rock cross plot. Green diamonds represent veins with calcite cement Cc1. Red squares represent veins with calcite cement Cc2. Δ represents the isotopic difference between calcite cements and carbonate host rocks.

Fig. 15 Detail of the Puig-reig anticline showing the trends in $\delta^{18}O$ and Fe^{2+} content in calcite cement Cc2. The $\delta^{18}O$ decreases and the Fe^{2+} content increases downwards the stratigraphic record. Minimum and maximum values are given.

Fig. 16 Conceptual models of the structural and fluid flow evolution of the Puig-reig anticline. Red, blue and green arrows indicate fluid movement. No vertical exaggeration. Fluid flow during the layer-parallel shortening. Hydrothermal fluids migrated along the main faults and more permeable sedimentary units. Below, fluid flow during fold growth. During this event, meteoric fluids circulated downwards the normal faults formed by outer arc extension and mixed with the hydrothermal fluids at depth.

Fig. 17 Fluid flow model of the northern part of the Ebro Basin. Red arrows indicate fluid migration of deep formation waters during T1 and T2. Blue arrows indicate fluid migration of shallow meteoric waters during T2. For sedimentary units legend see Fig. 2a.

Table 1

Sample	Description	Fault type	Cement generation	$\delta^{13}C$ VPDB	$\delta^{18}O$ VPDB
GP-R4	Palustrine-lacustrine carbonate	Strike-slip		-2.73	-7.26
302	Carbonate-derived clast	Strike-slip		-3.22	-4.70
303	Carbonate-derived clast	Strike-slip		3.11	-3.12
311F	Carbonate-derived clast	Strike-slip		1.22	-7.19
311G	Carbonate-derived clast	Strike-slip		-0.84	-8.91
312A	Carbonate-derived clast	Normal		0.59	-3.43
EM-1	Palustrine-lacustrine carbonate			-2.44	-6.92
PR-1A	Palustrine-lacustrine carbonate			-3.3	-7.28
PR-1B	Palustrine-lacustrine carbonate			-2.52	-7.22
GP-R1	Calcite shear vein	Strike-slip	Cc1	-1.51	-6.74
GP-R1	Calcite shear vein	Strike-slip	Cc1	-1.51	-6.85
GP-R1	Calcite shear vein	Strike-slip	Cc2	-1.44	-11.41
GP-R1	Calcite shear vein	Strike-slip	Cc2	-1.52	-11.06
GP-R1	Calcite shear vein	Strike-slip	Cc2	-1.34	-12.16
GP-R2	Calcite extension vein	Strike-slip	Cc1	-1.93	-6.67
GP-R2	Calcite extension vein	Strike-slip	Cc1	-1.91	-6.60
GP-R2	Intergranular cement	Strike-slip	Cc1	-1.07	-6.25
GP-R4	Vug porosity	Strike-slip	Cc1	-1.57	-6.37
GP-R4	Calcite shear vein	Strike-slip	Cc1	-1.22	-6.30
GP-R4	Calcite shear vein	Strike-slip	Cc1	-1.41	-6.25
GP-R5	Intergranular cement	Strike-slip	Cc1	0.53	-5.93
GP-R5	Calcite shear vein	Strike-slip	Cc2	-2.06	-10.67
GP-R5	Calcite shear vein	Strike-slip	Cc2	-2.05	-9.96
GP-R7	Calcite shear vein	Reverse	Cc1	-1.71	-6.29
GP-R7	Calcite shear vein	Reverse	Cc1	-1.79	-7.76
GP-R7	Intergranular cement	Reverse	Cc1	-0.62	-6.25
GP-R9A	Calcite extension vein	Strike-slip	Cc1	-0.59	-6.54
GP-R9A	Calcite shear vein	Strike-slip	Cc1	-0.78	-6.17
GP-R9A	Calcite shear vein	Strike-slip	Cc1	-0.82	-6.26
GP-R9A	Intergranular cement	Strike-slip	Cc1	-0.09	-6.72
GP-R9B	Calcite shear vein	Strike-slip	Cc1	-0.85	-6.54
GP-R9B	Intergranular cement	Strike-slip	Cc1	-0.02	-6.74
GP-R10	Calcite shear vein	Strike-slip	Cc1	-0.11	-6.76
GP-R11	Calcite shear vein	Strike-slip	Cc1	-1.08	-7.19
GP-R11	Calcite shear vein	Strike-slip	Cc1	-1.08	-6.69
GP-R11	Intergranular cement	Strike-slip	Cc1	-1.04	-6.69
GP-R11	Calcite shear vein	Strike-slip	Cc2	-1.61	-9.67
GP-R12	Intergranular cement	Normal	Cc1	-1.31	-7.53
GP-R12	Calcite shear vein	Normal	Cc2	-1.95	-9.63
GP-R12	Calcite shear vein	Normal	Cc2	-1.99	-9.62
GP-R13	Calcite shear vein	Strike-slip	Cc1	-1.37	-6.41
GP-R13	Calcite shear vein	Strike-slip	Cc1	-1.42	-6.44
GP-R13	Intergranular cement	Strike-slip	Cc1	-0.65	-6.23
302	Calcite extension vein	Strike-slip	Cc1	0.21	-8.02
302	Calcite shear vein	Strike-slip	Cc1	0.25	-8.02
302	Calcite shear vein	Strike-slip	Cc1	-0.51	-9.39
303	Calcite shear vein	Strike-slip	Cc1	0.10	-7.81
309A	Calcite shear vein	Strike-slip	Cc1	0.23	-7.29
309A	Calcite shear vein	Strike-slip	Cc1	0.11	-7.37
309B1	Calcite shear vein	Strike-slip	Cc1	-0.40	-7.36
309B1	Calcite shear vein	Strike-slip	Cc1	-0.40	-7.65
310	Calcite shear vein	Strike-slip	Cc1	0.96	-6.90
310	Calcite shear vein	Strike-slip	Cc1	0.75	-7.12
311A	Calcite shear vein	Strike-slip	Cc1	-0.69	-8.79
311A	Calcite shear vein	Strike-slip	Cc2	-0.73	-12.68
311A	Calcite shear vein	Strike-slip	Cc2	-2.13	-11.98
311B	Calcite shear vein	Strike-slip	Cc1	-0.67	-7.21
311B	Calcite shear vein	Strike-slip	Cc1	-1.30	-9.09
311D	Calcite shear vein	Strike-slip	Cc2	-0.95	-13.07
311D	Calcite shear vein	Strike-slip	Cc2	-0.51	-12.46
311F	Calcite shear vein	Strike-slip	Cc1	0.74	-7.05
311F	Calcite shear vein	Strike-slip	Cc1	0.74	-7.07
311G	Calcite shear vein	Strike-slip	Cc2	0.19	-12.99
312A	Calcite shear vein	Normal	Cc1	0.63	-7.57
312A	Calcite shear vein	Normal	Cc2	0.02	-13.11

313A	Calcite shear vein	Normal	Cc2	-1.40	-12.88
313A	Calcite shear vein	Normal	Cc2	-1.80	-13.30
313A’	Calcite shear vein	Normal	Cc1	-2.34	-7.59
313A’	Calcite shear vein	Normal	Cc2	-2.30	-11.14
314A	Small fracture affecting clasts	Normal	Cc1	0.15	-7.50
314A	Calcite shear vein	Normal	Cc2	-1.60	-13.10
314A	Calcite shear vein	Normal	Cc2	-0.95	-10.64
314B	Calcite shear vein	Strike-slip	Cc1	0.00	-7.23
314B	Calcite shear vein	Strike-slip	Cc1	0.05	-7.23
314C	Calcite shear vein	Strike-slip	Cc1	-0.22	-7.41
314C	Calcite shear vein	Strike-slip	Cc1	-0.23	-7.83
314D1	Calcite shear vein	Normal	Cc1	-1.11	-7.85
314D1	Calcite shear vein	Normal	Cc2	-1.79	-12.80
314D2	Calcite shear vein	Normal	Cc1	-1.34	-9.27
314D2	Calcite shear vein	Normal	Cc2	-1.47	-13.95
314D2	Calcite shear vein	Normal	Cc2	-2.46	-12.21
317	Calcite shear vein	Strike-slip	Cc1	-1.23	-8.09
317	Calcite shear vein	Strike-slip	Cc1	-1.34	-7.50

Table 2

Sample	Cement type	n	$\delta^{13}C$ VPDB	$\delta^{18}O$ VPDB	Δ_{47}	T ºC	$\delta^{18}O_{fluid}$ VSMOW
309B1	Cc1	3	-0.44	-7.77	0.548 ± 0.009	92 ± 5	4.7 ± 0.6
317	Cc1	3	-0.99	-6.95	0.494 ± 0.010	129 ± 8	9.2 ± 0.7
311A	Cc2	3	-0.77	-12.32	0.574 ± 0.010	77 ± 5	-1.7 ± 0.7
311D	Cc2	3	-0.73	-12.85	0.551 ± 0.004	90 ± 3	-0.7± 0.3

Table 3

Sample	Description	Fault type	Cement generation	$^{87}Sr/^{86}Sr$
GP-R4	Eocene-Oligocene host-mudstone	Strike-slip		0.708865
IP-R	Eocene-Oligocene host-marly limestone			0.708967
309A	Calcite shear vein	Strike-slip	Cc1	0.709246
311A	Calcite shear vein	Strike-slip	Cc2	0.708947
311D	Calcite shear vein	Strike-slip	Cc2	0.709002
314C	Calcite shear vein	Strike-slip	Cc1	0.709138

Table 4

Filling stage	n	Analysed samples		Mg (ppm)	Mn (ppm)	Fe (ppm)	Sr (ppm)
Calcite	45	GP-R1					
cement		GP-R4					
Cc1		309A	Min.	600	600	<d.l.	<d.l.
		311A	Max.	4500	2800	1100	600
		314D2	Av.	2171	1406	544	537
Calcite	45	GP-R1					
cement		311A					
Cc2		311D	Min.	<d.l.	300	300	<d.l.
		312D2	Max.	2400	2300	3200	3000
			Av.	1038	1268	1080	886

Table 1 $\delta^{18}O$ and $\delta^{13}C$ values of the host-carbonates and calcite cements Cc1 and Cc2. For the third and fourth columns, the blank spaces represent host rock samples which are not affected by faults and do not contain calcite cement, respectively.

Table 2 Calcite cement $\delta^{13}C$, $\delta^{18}O$, Δ_{47} and $\delta^{18}O_{fluid}$. n represents the number of analyses per sample.

Table 3 $^{87}Sr/^{86}Sr$ values of palustrine-lacustrine host-carbonates and calcite cements Cc1 and Cc2. For the third and fourth columns, the blank spaces represent host rock samples which are not affected by faults and do not contain calcite cement, respectively.

Table 4 Minimum, maximum and average values of the elemental composition of the calcite cements Cc1 and Cc2. n represents the number of analyses per calcite cement generation. For fault types affecting the analyzed samples see Table 1.